1 **Emission-dominated gas exchange of elemental mercury vapor over natural surfaces in China**

2 Xun Wang[1,2], Che-Jen Lin[1,3,4,*], Wei Yuan[1,2], Jonas Sommar [1], Wei Zhu [1], Xinbin Feng[1,*]

4 [1] State Key Laboratory of Environmental Geochemistry, Institute of Geochemistry, Chinese Academy of
5 Sciences, Guiyang, China
6 [2] University of Chinese Academy of Sciences, Beijing, China
7 [3] Center for Advances in Water and Air Quality, Lamar University, Beaumont, TX, USA
8 [4] Department of Civil and Environmental Engineering, Lamar University, Beaumont, TX, USA

10 **\* Corresponding Authors:**

11 Xinbin Feng                                  Che-Jen Lin
12 Phone: +86-851-5895728              Phone: +1 409 880-8761
13 Fax + 86-851-5891609                   Fax: +1 409 880-8121
14 Email: fengxinbin@vip.skleg.cn       E-mail: Jerry.Lin@lamar.edu

16 **Abstract**: Mercury (Hg) emission from natural surfaces plays an important role in global Hg cycling. The
17 present estimate of global natural emission has large uncertainty and remains unverified against field data,
18 particularly for terrestrial surfaces. In this study, a mechanistic model is developed for estimating the
19 emission of elemental mercury vapor ($Hg^0$) from natural surfaces in China. The development implements
20 recent advancements in the understanding of air-soil and air-foliage exchange of $Hg^0$ and redox chemistry
21 in soil and on surfaces, incorporates the effects of soil characteristics and landuse changes by agricultural
22 activities, and is examined through a systematic set of sensitivity simulations. Using the model, the net
23 exchange of $Hg^0$ between the atmosphere and natural surfaces of Mainland China is estimated to be 465.1
24 Mg $yr^{-1}$, including 565.5 Mg $yr^{-1}$ from soil surfaces, 9.0 Mg $yr^{-1}$ from water body, and -100.4 Mg $yr^{-1}$ from
25 vegetation. The air-surface exchange is strongly dependent on the landuse and meteorology, with 9% of net
26 emission from forest ecosystems, 50% from shrubland, and savanna and grassland, 33% from cropland,
27 and 8% from other landuses. Given the large agricultural land area in China, farming activities play an
28 important role on the air-surface exchange over farmland. Particularly, rice field shift from a net sink (3.3
29 Mg uptake) during April to October (rice planting) to a net source when the farmland is not flooded
30 (November-March). Summing up emissions from each landuse, more than half of the total emission occurs
31 in summer (51%), followed by spring (28%), autumn (13%) and winter (8%). Model verification is
32 accomplished using observational data of air-soil/air-water fluxes and Hg deposition through litterfall for
33 forest ecosystems in China and Monte Carlo simulations. In contrast to the earlier estimate by Shetty et al.
34 (2008) that reported large emission from vegetative surfaces using an evapotranspiration approach, the
35 estimate in this study shows natural emissions are primarily from grassland and dry cropland. Such an
36 emission pattern may alter the current understanding of Hg emission outflow from China as reported by
37 Lin et al. (2010b) because of a substantial natural Hg emission occurs in West China.

## 1. Introduction

Accurate inventories of mercury (Hg) emission is the foundation for assessing Hg global biogeochemical cycling (Selin, 2009;Streets et al., 2009;Streets et al., 2011). The inventories of Hg emission include the emission from anthropogenic sources, and the so-called "natural" emission that includes the primary natural release (i.e., from geogenic activities) and the re-emission of legacy Hg stored in the terrestrial and water surfaces. Hg emission from anthropogenic sources has been quantified and updated with reasonable consistency since the 1990s (Streets et al., 2009;Streets et al., 2011;Zhang et al., 2015;Zhang et al., 2016). In particular, the inclusion of the release from commercial products and modifications of Hg emission speciation profiles corresponding to the implementation and upgrade of air pollution control technologies have substantially reduced the uncertainty of anthropogenic Hg emission estimates (Horowitz et al., 2014;Zhang et al., 2016). In contrast, estimates of natural Hg emission are poorly constrained and have large uncertainties ($\pm 2000$ Mg yr$^{-1}$), limiting the understanding of global and regional Hg cycling budgets (Pirrone et al., 2010;Wang et al., 2014b;Song et al., 2015). In light of the control of anthropogenic Hg emission by the legally binding Minamata Convention (Pacyna et al., 2016), a better quantification of natural Hg emission is critical in evaluating the effectiveness of policy actions (Selin, 2009;Pirrone et al., 2010;Song et al., 2015).

One of the greatest challenges in predicting natural Hg emissions is the limited understanding in the air-surface Hg$^0$ exchange processes among multiple environmental compartments, such as those in a terrestrial vegetative ecosystem. Estimates from regression-based models derived from the correlations between Hg flux and environmental parameters (e.g., temperature, solar radiation, etc.) may not be representative (Xu et al., 1999;Bash et al., 2004;Lin et al., 2005;Gbor et al., 2006;Shetty et al., 2008;Selin et al., 2008;Smith-Downey et al., 2010) because the relationships between measured fluxed and environmental factors are based on limited field data that are be site-specific, which cannot account for the heterogeneity in soil properties and vegetative coverages. Although the bidirectional resistance schemes describing Hg$^0$ gas exchange may be appropriate (Bash, 2010;Wang et al., 2014b;Wright and Zhang, 2015), they are limited by the availability of required soil property data and other physicochemical parameters such as Hg$^{II}$ reduction kinetics and characteristics of interfacial exchanges (Bash, 2010;Wang et al., 2014b),

leading to inconsistences between simulated and measured fluxes. Other challenges including acquiring and integrating the meteorology, landuse, and soil property data (Hg content and other characteristics) in a model domain covering China call for further model development to estimate natural Hg emission (Wang et al., 2014b).

Recent advances in the understanding of $Hg^{II}$ reduction provide new opportunities to build a more physically robust air-soil exchange scheme. These include constrained $10^{-11}$ to $10^{-10}$ $s^{-1}$ pseudo-first-order rate constant of $Hg^{II}$ reduction in soil (Scholtz et al., 2003;Qureshi et al., 2011) and 0.2-1.0 $h^{-1}$ rate constant in natural water (O'Driscoll et al., 2006;Qureshi et al., 2010). In these reactions, the UV-band of actinic light has been shown to be the primary driver for $Hg^{II}$ photo-reduction in soils and water bodies (Moore and Carpi, 2005;Si and Ariya, 2011); and the role of functional substructures (e.g., -C(O)OH, -SH, -OH) of DOM (dissolved organic matter) in the reduction has been determined by kinetic studies using model compounds (He et al., 2012;Si and Ariya, 2011, 2015). Presence of dissolved $O_2$ has been shown to inhibit most aqueous $Hg^{II}$ reduction but not the photo-reduction of $Hg^{II}$ bound to R-SH (Si and Ariya, 2011). In dry soil, the first-order rate constants of $Hg^{II}$ photo-reduction are 0.007-0.028 $h^{-1}$ for $HgCl_2$ coated over sand and 0.003-0.006 $h^{-1}$ for $Hg^{II}$ in a natural soil (Quinones and Carpi, 2011). In the absence of light, $Hg^{II}$ reduction in soil is also observed at a rate of 0.001-0.002 $h^{-1}$ at 293 K (Pannu, 2012).

Intercontinental transport of Hg emission in China has been suggested to enhance Hg deposition in North America (Jaffe et al., 2005;Strode et al., 2008;Lin et al., 2010b;Chen et al., 2014). However, the natural Hg emission inventory used in earlier modeling studies may not be representative. Wang et al. (2014a) suggested the Hg emissions in China from natural and anthropogenic sources are comparable. Shetty et al. (2008) estimated the natural Hg emission in China to be 462 Mg $yr^{-1}$ using an outdated model scheme, which was applied for assessing regional Hg budgets in Est Asia (Lin et al., 2010b;Zhu et al., 2015a). The large uncertainty associated with the earlier estimate warrants a re-assessment of these earlier modeling efforts. In addition, the data of soil Hg concentration used in Shetty et al. (2008) are more than 3 decades old and requires updates to appropriately represent spatial distribution of soil Hg contents that have been modified due to the rapid industrial development and urbanization occurring in China since 1980s. This data deficiency has been addressed by the National Multi-Purpose Regional Geochemical Survey

(NMPRGS) of China completed in 2014 (Li et al., 2014). This database provides soil Hg content for the agricultural and industrialized regions at a resolution of 4 km, which may substantially reduce uncertainty caused by data deficiency. In addition, the datasets of terrestrial flux in Mainland China recently reported in the literature allows verification of model results and optimization of model schemes. These field data of $Hg^0$ air-surface exchange in China documents the flux characteristics over different landuses including urban-rural-remote differences and effects of crop rotation over agricultural lands (Fu et al., 2008;Fu et al., 2010;Zhu et al., 2011;Fu et al., 2012;Fu et al., 2013a;Sommar et al., 2013a;Sommar et al., 2013b;Zhu et al., 2013;Sommar et al., 2015a;Zhu et al., 2016).

Given the scientific advancements and new data availability discussed above, this work develops a state-of-the-science mechanistic model for estimating the natural Hg emission in China. For the first time, the simulated natural emission flux is verified with field measurements over different land surfaces in a modeling effort. The spatial, temporal and seasonal characteristics of the model-estimated emissions over soil, vegetative surface and water are presented and compared to the earlier estimates performed by Shetty et al. (2008). The implications of the new estimate are discussed in terms of chemical transport of Hg emission in China and the need for a re-assessment of mercury emission outflow from China.

## 2. Methods

### 2.1 Model description

Compared to the earlier mechanistic schemes (Wang et al., 2014b;Bash, 2010;Scholtz et al., 2003;Zhang et al., 2012b), this model (1) builds a new scheme for estimating the air-soil flux based on the reduction pathways of reactive Hg in soil identified in the literature, (2) develops a scheme for the Hg flux exchange over rice paddy, which is an important landuse feature in China, and (3) updates the scheme for the air-snow interface and chemical parameters for air-foliage flux (Table 1).

### 2.1.1 Reduction of $Hg^{II}$ in soil

Based on $Hg^{II}$ reduction mechanisms proposed in peer-reviewed literature (Moore and Carpi, 2005;Quinones and Carpi, 2011;Si and Ariya, 2011;Pannu, 2012), a new model describing $Hg^0$ formation from $Hg^{II}$ reduction in soil is developed using three reaction pathways: (1) photo-reduction of $Hg^{II}$ in soil

120 pore water ($Hg_1^0$), (2) photo-reduction of Hg$^{II}$ associated with soil particles ($Hg_2^0$), and (3) Hg$^{II}$ reduction

121 through non-photochemical pathways ($Hg_3^0$). The production of Hg$^0$ in surface soil is calculated as:

122 $$\frac{dHg_1^0}{dt} = K_1 \cdot Hg_{s,m} \qquad (1)$$

123 $$\frac{dHg_2^0}{dt} = K_2 \cdot Hg_{p,m} \qquad (2)$$

124 $$\frac{dHg_3^0}{dt} = K_3 \cdot Hg_{t,m} \qquad (3)$$

125 where $K_1$ is the photo-reduction rate constant of Hg$^{II}$ in soil pore water (a comprehensive parameter list with

126 units is shown in Table 1), $K_2$ is the photo-reduction rate constant of Hg$^{II}$ associated with soil particles, $K_3$

127 is the Hg$^{II}$ reduction rate constant in soil through non-photochemical pathways, $Hg_{s,m}$ is the Hg$^{II}$ pool in soil

128 pore water, $Hg_{p,m}$ is the labile Hg$^{II}$ pool available for reduction on soil particles, $Hg_{t,m}$ is the total reducible

129 Hg$^{II}$ pool in soil. Based on the Arrhenius equation, $K_1$ and $K_2$ are parameterized as a function of solar

130 irradiance and soil temperature, and $K_3$ is parameterized as a function of soil temperature and soil moisture:

131 $$K_1 = k_1 \cdot R \cdot \gamma \cdot e^{\frac{T-T_f}{T_f} \cdot \frac{E_a}{T}} \qquad (4)$$

132 $$K_2 = k_2 \cdot R_i \cdot \gamma \cdot e^{\frac{T-T_f}{T_f} \cdot \frac{E_a}{T}} \qquad (5)$$

133 $$K_3 = k_3 \cdot e^{\frac{T-T_f}{T_f} \cdot \frac{E_a}{T}} \cdot e^{\frac{\theta-\theta_f}{\theta_f} \cdot \frac{E_b}{\theta}} \qquad (6)$$

134 where $k_1$ and $k_2$ are the photo-reduction rate constants at the reference soil temperature ($T_f$, Table 1). $k_3$ is

135 the dark-reduction rate constant at the reference soil temperature and soil moisture ($\theta_f$, Table 1). $R$ and $R_i$

136 are total solar irradiance in the soil profile and under the canopy, respectively. $\gamma$ is the ratio of UV over

137 total solar irradiance. An empirical rule suggests that a 10°C temperature increase doubles the rates for

138 chemical reactions near room temperature (Kissinger, 1957;Hood et al., 1975), which has been shown to

139 be applicable to Hg$^{II}$ reduction in boreal soil (Pannu et al., 2014). In addition, Hg emission flux from soil

140 substrate doubles at ~25% increase of soil moisture content (Lin et al., 2010a). Based on these observations,

141 Equations 4-6 can be simplified as:

142 $$K_1 = k_1 \cdot R \cdot \gamma \cdot 2^{\frac{T-T_f}{10}} \qquad (7)$$

143 $$K_2 = k_2 \cdot R_i \cdot \gamma \cdot 2^{\frac{T-T_f}{10}} \qquad (8)$$

144 $$K_3 = k_3 \cdot 2^{\frac{T-T_f}{10}} \cdot 2^{\frac{\theta-\theta_f}{25\%}} \qquad (9)$$

145 $R$ and $R_i$ in Equations 7-8 are calculated based on the Beer-Lambert law:

146 $$R_i = R_0 \cdot e^{-K \cdot LAI} \qquad (10)$$

147 $$R = R_i \cdot \int_0^l e^{-k_r \cdot l} dl \qquad (11)$$

148 where $R_0$ is solar irradiance above the canopy, $K$ is the canopy light extinction coefficient, $LAI$ is leaf area

149 index, $k_r$ is the light extinction coefficient in soil, $l$ is the depth of surface soil.

150 $Hg_{s,m}$ and $Hg_{p,m}$ and $Hg_{t,m}$ are calculated based on Lyon et al. (1997):

151 $$Hg_{s,m} = \frac{[Hg_t] \cdot BD}{\theta + kd \cdot BD} \cdot V \cdot \theta \cdot 10^6 \qquad (12)$$

152 $$Hg_{p,m} = \frac{[Hg_t] \cdot BD \cdot kd}{\theta + kd \cdot BD} \cdot BD \cdot V \cdot \varphi \qquad (13)$$

153 $$Hg_{t,m} = [Hg_t] \cdot BD \cdot V \cdot \varphi \qquad (14)$$

154 where $[Hg_t]$ is the total Hg$^{II}$ concentration in soil, $BD$ is the soil bulk density, $\theta$ is the soil moisture, and

155 $V$ is the soil volume, $\varphi$ is the ratio of reducible Hg over total Hg in soil. $kd$ is the soil-water partition

156 coefficient and calculated following Lee et al. (2001) and Sauve et al. (2000):

157 $$\log kd = r \cdot pH + s \cdot \log(1000 \cdot foc) + t \qquad (15)$$

158 where $f_{oc}$ is the fraction of organic carbon in surface soil. The values $r, s$ and $t$ are regression coefficients.

159 Following Obrist et al. (2014), we assume that the Hg$^0$ emission from soil is controlled by diffusion

160 after Hg$^{II}$ reduction. Basing on the Fick's first law, the observed air-soil flux exchange can be calculated as:

161 $$F_{soil} = Hg_1^0 + Hg_2^0 + Hg_3^0 - D_{soil} \frac{GEM}{d/2} \Delta t \qquad (16)$$

162 $$D_{soil} = 0.66 \cdot (\sigma - \theta) \cdot D_0 \qquad (17)$$

163 where $D_{soil}$ and $D_0$ are the diffusivities of Hg$^0$ vapor in soil and ambient air. GEM is the atmospheric Hg$^0$

164 concentration, $\sigma$ is the soil porosity. Hence, during a time period $\Delta t$, the soil Hg$^0$ vapor compensation

165 point used in the bidirectional resistance model can be derived as:

166 $$\chi_g = \frac{(Hg_1^0 + Hg_2^0 + Hg_3^0) \cdot d/2}{D_{soil} \cdot \Delta t} \qquad (18)$$

167

168 **2.1.2 Updates for air-terrestrial exchanges**

169      Extending from the two categories (vegetated canopy and bare land) from our earlier work (Wang et

170      al. (2014b), the terrestrial system is divided into four categories: vegetated surface with unsaturated soil

171      moisture (e.g., forest, grassland, shrubland, etc.), vegetated surface with saturated soil (i.e., rice paddy),

172      barren or sparsely vegetated land, and snow/ice surface. The governing equation for calculating $Hg^0$ air-

173      surface exchange over vegetated surfaces is:

174      $F_{cnp} = \frac{\Delta t}{(R_a + R_b)} (\chi_{cnp} - C_{atm})$           (19)

175      where $R_a$ is the aerodynamic resistance,  $R_b$ is the quasi-laminar sub-layer resistance, $C_{atm}$ is the

176      atmospheric Hg concentration, $\chi_{cnp}$ is the overall compensation point. For the canopy biomes with

177      unsaturated soil, $\chi_{cnp}$ is parameterized as in Wang et al. (2014b):

178      $\chi_{cnp} = \frac{\frac{\chi_c}{R_c} + \frac{\chi_s}{R_s} + \frac{\chi_g}{R_g + R_{ac}} + \frac{C_{atm}}{R_a + R_b}}{\frac{1}{R_c} + \frac{1}{R_s} + \frac{1}{R_g + R_{ac}} + \frac{1}{R_a + R_b}}$           (20)

179      where $\chi_c$ is the cuticular compensation point, $\chi_s$ is the stomatal compensation point, $R_c$ is the cuticular

180      resistance, $R_s$ is the stomatal resistance, $R_g$ is the soil diffusion resistance, $R_{ac}$ is the in-canopy

181      aerodynamic resistance (Table 1 in details). While for vegetated surface with saturate soil, $\chi_{cnp}$ is

182      parameterized as following:

183      $\chi_{cnp} = \frac{\frac{\chi_c}{R_c} + \frac{\chi_s}{R_s} + \frac{\chi_w}{R_w + R_{ac}} + \frac{C_{atm}}{R_a + R_b}}{\frac{1}{R_c} + \frac{1}{R_s} + \frac{1}{R_w + R_{ac}} + \frac{1}{R_a + R_b}}$           (21)

184      where $\chi_w$ is the air-water compensation point, $R_w$ is the diffusional resistance on water surface.

185      The governing equation for air-surface exchange in barren or sparsely vegetated land, and over

186      snow/ice surface is:

187      $F_{bls} = \frac{\Delta t}{R_a + R_b + R_g} (\chi_g - C_{atm})$           (22)

188      For bare land, $R_g$ is calculated following Zhang and Lindberg (1999):

189      $R_g = \frac{d/2}{0.66 \cdot (\sigma - \theta) \cdot D_0}$           (23)

190      For snow/ice surface, $R_g$ is evaluated following Zhang et al. (2012b):

191      $\frac{1}{R_g} = \frac{\alpha_{Hg^0}}{R_{g(SO_2)}} + \frac{\beta_{Hg^0}}{R_{g(O_3)}}$           (24)

192 where $R_{g(SO_2)}$ and $R_{g(O_3)}$ are the diffusion resistances of SO$_2$ and O$_3$, $\alpha_{Hg^0}$ is the Hg$^0$ scaling factor

193 based on SO$_2$, $\beta_{Hg^0}$ is Hg$^0$ scaling factor based on O$_3$. The formulation of $R_{g(SO_2)}$ and $R_{g(O_3)}$ has been

194 described previously (Zhang et al., 2003;Wang et al., 2014b). The $\chi_g$ for the air-snow interface is assumed

195 to be 3 ng m$^{-3}$ based on field measurements at air-snow interface (Mann et al., 2015;Lalonde et al.,

196 2003;Fain et al., 2007;Maxwell et al., 2013). Other parameters in Equations 19-24 are described in details

197 in Wang et al. (2014b).

**2.2 Model configuration and data**

199      The modeling domain is in Lambert Conformal projection, with 223×149 grid cells at a 36-km spatial

200 resolution. The modeling period is one year (2013). Hourly meteorological data are prepared using the

201 Weather Research and Forecasting (WRF) model Version 3.7. Sensitivity analysis in Wang et al. (2014b)

202 showed that accurate representation of environmental parameters (e.g., temperature, solar irradiance, etc.)

203 greatly improves the flux estimate. To obtain the best physics and dynamics options of WRF for the China

204 domain, a L$_{25}$ (5$^6$) orthogonal design of experiments is utilized (Supplementary material, Table **S1**). The

205 best combination of meteorological physics options is selected based on model evaluation metrics R

206 (correlation coefficient) and RMSE (root-mean-square error) between simulated outputs of each

207 combination of options and observed values in 750 meteorological stations. The selected physics options

208 are Thompson (Microphysics Options), Betts-Miller-Janjic (Cumulus Parameterization Options), RRTMG

209 (Radiation Physics Options) and BouLac (PBL Physics Options) based on the results of meteorological

210 model performance evaluation (Figure **S1**).

211      The datasets for surface soil properties (1 km spatial resolution) containing organic matters contents,

212 pH, bulk density and porosity are adopted from Shangguan et al. (2013). The land cover data (1 km spatial

213 resolution) is obtained from Ran et al. (2012). The land cover map represents the best available datasets

214 and follows the IGBP (International Geosphere-Biosphere Programme) classification system (Figure **S2**).

215 The ratio of rice planting fields in China during each month are classified following the method used in Liu

216 et al. (2013). The rice planting seasons are April to October in South China (including double rice planting),

217 and May to October in Northeast China (single rice planting). The LAI data, also with a 1 km spatial

218 resolution, are adopted from Yuan et al. (2011). The soil Hg content information utilized by Shetty et al.

219 (2008) is updated and greatly expanded with the comprehensive NMPRGS dataset (Li et al., 2014). These

220 high resolution datasets were re-gridded into the domain specification for each landuse using the spatial

221 tools in ArcGIS 10.1. The soil Hg content in 0-20 cm surface soil varies with landuse types, containing

222 mean concentrations of 119~211, 61~197, 80~82, 80~82 and 31~162 ng g$^{-1}$ of Hg for forest ecosystems,

223 shrubland, savanna/grassland, cropland, and other landuses, respectively (Table 1). Though the mean Hg

224 concentration in 0-20 cm soil profile could somewhat underestimates Hg concentration in the top soil layer,

225 the dataset is the best available one describing the soil Hg concentration in China. Datasets of Hg

226 concentration in the top soil layer (e.g., 0-5 cm depth) are recommended when they become available.

227 In the simulation, the validated Hg$^0$ concentration retrieved from the output of the Hg extension of

228 Community Multi-scale Air Quality modeling system (CMAQ-Hg) version 4.7 for the same modeling

229 period is applied to represent the ambient air concentration of Hg$^0$ (Lin et al., 2010b). The simulation does

230 not incorporate the feedback of the air-surface exchange to the air concentration because the feedback of

231 the air-surface exchange to the air concentration does not significantly modify the atmospheric Hg$^0$

232 concentration in each grid cell, and the typical variation range of ambient Hg$^0$ concentration is not a

233 sensitivity parameter for flux change (Wang et al., 2014b). The model algorithms are coded in FORTRAN

234 90 and Network Common Data Form (NetCDF) version 4.3. The gridded model results are visualized by

235 the Visualization Environmental for Rich Data Interpretation (VERDI) version 1.5.

236

237 **3 Results and discussion**

238 **3.1 Evaluation for soil Hg reduction scheme**

239 Values of all model parameters used in the simulation are showed in Table 1. The value of $k_1$ is assumed

240 to be $6 \times 10^{-9}$ m$^2$ W$^{-1}$ s$^{-1}$ based on the relationship between irradiance intensity and apparent photo-reduction

241 rate constant in aerated solution observed by Si and Ariya (2011). Considering the 2 mm maximum

242 photolysis penetration depth in soil (Hebert and Miller, 1990), the measured rate constant in soil particles

243 (depth = 2.07 mm) from Quinones and Carpi (2011) is $2 \times 10^{-3}$ m$^2$ W$^{-1}$ h$^{-1}$ ($k_2$) with respect to the pool of

244 labile Hg$^{II}$ available for reduction. The value of $k_3$ is assumed to be $1.0 \times 10^{-3}$ h$^{-1}$ based on the average rate

245 constants for dark (thermal) reduction (Pannu, 2012). The mean ratio of reducible Hg in soil is assumed to

246 be 0.03 for the soil with vegetation based on measurements from Pannu (2012). No data is available for the

247 bare soil. Data from Lindberg et al. (1999) imply that Hg-enriched desert soil (1400-5000 ng $g^{-1}$ total Hg)

248 produces a nominal $Hg^0$ efflux in the range from 40 to 60 ng $m^{-2}$ $h^{-1}$. Derived from back-calculation taking

249 pore diffusion into account, the fraction of reducible Hg is predicted at least 10 times lower ($\leq 0.003$) than

250 that in the soil with vegetation.

251 Sensitivity analyses using a box model for a typical forest soil are performed to gauge the selected rate

252 coefficients and the results are showed in Figure 2. With $k_1 = 6.0 \times 10^{-9}$ $m^2$ $W^{-1}$ $s^{-1}$, $k_2 = 2.0 \times 10^{-3}$ $m^2$ $W^{-1}$ $h^{-1}$,

253 $k_3 = 1.0 \times 10^{-3}$ $h^{-1}$, the $Hg^0$ vapor concentration in soil porous media is estimated to be 4.5 ng $m^{-3}$, comparable

254 to the measured concentration ($4.1 \pm 2.0$ ng $m^{-3}$) in the surface forest floor (Moore and Castro, 2012). This

255 suggests that the selected empirical constants appropriately represent typical environmental conditions.

256 Generally, the range of $Hg^0$ vapor in all simulations is 1.5-6.7 ng $m^{-3}$. Less than 0.1% $Hg^0$ vapor is from

257 photo-reduction in soil solution as the Hg pool in soil solution is small ($\leq 0.1\%$ of total Hg concentration).

258 A ~16% fraction of the pore $Hg^0$ concentration derives from thermal $Hg^{II}$ reduction, contributing to 0.5-1

259 ng $m^{-3}$ of $Hg^0$ vapor present in soil gas. Hg⁰ concentrations in pore gas are typically lower than the 1-2 ng

260 m⁻³ atmospheric Hg concentration in background forest at night (Carpi and Lindberg, 1998;Ericksen and

261 Gustin, 2006;Kuiken et al., 2008a;Kuiken et al., 2008b;Obrist et al., 2014;Fu et al., 2015), suggesting that

262 forest floor acts as a $Hg^0$ sink during nighttime. This is consistent with the sign of nocturnal fluxes observed

263 over forest floor (Carpi and Lindberg, 1998;Ericksen et al., 2006;Kuiken et al., 2008a;Kuiken et al., 2008b).

264 Moore and Carpi (2005) reported that the Hg flux under sun-lit condition is 3-5 times higher than the value

265 observed in the dark. The developed model is capable of producing results consistent with the observation

266 that photo-reduction on soil particles dominates the formation of $Hg^0$ vapor.

267 Figure 3 illustrates the model response to the model variables at the two experimental levels in Table

268 2. The 2-level factorial design of experiments is meant to gauge the extreme variation of flux caused by the

269 possible range of all parameters. This method is statistically robust, and therefore the synergistic and

270 antagonistic interactions among model parameters can be estimated with indications of statistical

271 significance. On average, increasing soil bulk density from 0.1 to 1.5 g $cm^{-3}$, and Hg content from 10 to

272 400 ng $g^{-1}$, and soil temperature from 0 to 30 ˚C, and solar radiation from 0 to 1000 W $m^{-2}$, will significantly

273    enhance the flux by 20-30 ng $m^{-2}$ $h^{-1}$. Additional 18-20 ng $m^{-2}$ $h^{-1}$ synergistic effects from the combination

274    of above parameters are also predicted. Filed measurements suggest the combined effects of soil Hg content

275    (from 60 to 590 ng $g^{-1}$) and soil temperature (from 5 to 30 ˚C) enhance the flux by ~40 ng $m^{-2}$ $hr^{-1}$ (Fu et

276    al., 2012;Fu et al., 2008). On the other hand, increasing leaf area index (LAI) from 0 to 7 $m^2$ $m^{-2}$ reduces

277    the flux by 19 ng $m^{-2}$ $h^{-1}$. Furthermore, LAI could offset the positive effects from bulk density, soil Hg

278    concentration, and solar radiation above canopy, leading to an additional -19 to -16 ng $m^{-2}$ $h^{-1}$ decrease,

279    indicating that the canopy shading substantially constrains soil Hg evasion, consistent with the shading

280    could decrease 70-90% fluxes compared to non-shaded soils in filed measurements (Carpi and Lindberg,

281    1998;Zhang et al., 2001;Choi and Holsen, 2009). In reality, since the actual variation of the parameters is

282    much smaller than the possible range, the flux change will also be much milder. To illustrate this, we run

283    the model using the center values of selected parameters (i.e., showing the model results by running the

284    model at half of the experimental level). Using the center values of soil Hg content, LAI, soil bulk density,

285    solar radiation and soil temperature in Table 2 (close to the environmental parameters in a typical forest

286    ecosystem), the air-soil flux is 4.5 ng $m^{-2}$ $hr^{-1}$, similar to the measures fluxes (0.5-9.3 ng $m^{-2}$ $hr^{-1}$) in forest

287    ecosystems of China (Fu et al., 2012;Fu et al., 2008).

288        In the new scheme, the soil organic matter is not incorporated into either $K_2$ or $K_3$, in accordance with

289    the findings of Pannu (2012). While $Hg^0$ evasion from substrates coated with $HgCl_2$ and humic matter is

290    inversely correlated with humic matter content both in the dark and under irradiation, the inhibitory effect

291    from humic matter is not linear to its content (Mauclair et al. (2008). For instance, relatively small

292    differences are observed at humic matter content > 1% (Mauclair et al., 2008). In addition, the effect of soil

293    organic matter type has not been comprehensively investigated (Zhang and Lindberg, 1999;Bash et al.,

294    2007). Further studies that quantify the reduction rate constants associated with different types of soil

295    organic matters (or species) under light, as well as field flux data that relate the observed flux intensity to a

296    given type of organic matter, can improve the present model parameterization.

297

298    **3.2 Diurnal variation of natural $Hg^0$ emissions in China**

299     Table 3 shows the annual mean air-surface fluxes for different landuse types. Annual mean air-foliage

300     fluxes range from -0.2 to -4.5 ng m$^{-2}$ h$^{-1}$, with the highest value over the woody savannas, and the lowest

301     over deciduous forests (Table 3). The diurnal variation for air-foliage flux is displayed in Figure 4. Higher

302     deposition occurs during mid-morning (8:00-10:00) and late-afternoon (16:00-17:00) due to the suitable air

303     temperature and solar irradiance that induces Hg uptake by stomata. The rates of Hg uptake during midday

304     are comparatively weaker due to the stronger irradiance and higher temperature. This bimodal pattern is

305     consistent with field observations (Lindberg et al., 2002;Poissant et al., 2008;Fritsche et al., 2008;Sommar

306     et al., 2015a), suggesting that the model is capable of simulating the diurnal pattern of air-foliage exchange

307     of Hg$^0$. Such a diurnal pattern is caused by re-emission of the deposited Hg on the surface foliage through

308     photo-reduction under the strong solar radiation during noontime, and the emissions from underlying soil

309     surfaces. Except for urban lands, the strength of diurnal deposition for the other landuses is controlled by

310     LAI, solar radiation, and air temperature. The elevated atmospheric Hg concentration is an important

311     parameter to induce Hg uptake by growing foliage in urban lands.

312     Simulated mean air-soil fluxes range from 0.1 to 23.3 ng m$^{-2}$ h$^{-1}$, with the lowest flux over barren

313     vegetated lands and the highest over urban lands (Table 3). This suggests that the simulated air-soil fluxes

314     greatly vary over different landuses. There are distinct diurnal variations in terrestrial ecosystems (Figure

315     5). The diurnal pattern is caused by the variation of solar irradiance, close to zero at night and peaking at

316     13:00 to 15:00 (UTC+8). Similar diurnal patterns have been observed during filed measurements for forest,

317     grassland, and cropland in China (Feng et al., 2005;Fu et al., 2008;Fu et al., 2012;Zhu et al., 2013). The

318     degree of diurnal variability for each landuse is highly related to the LAI. Higher LAI gives a more intensive

319     canopy shading and largely inhibits Hg evasion from soil under canopy. This is also the main reason for

320     relative weaker diurnal variation over forest soils compared to shrubland, grassland and cropland (Figure

321     5). The synergistic interactions between low vegetation cover and high soil concentration (Mean=162±83

322     ng g$^{-1}$) results in the strongest diurnal variation for urban land-types.

323     The simulated annual mean of air-water flux is 3.4 ng m$^{-2}$ h$^{-1}$. The diurnal variability for air-water flux

324     is weaker since wind speed is a more influential driver than irradiance (Wang et al., 2014b), consistent with

325     the diurnal variation observed in field studies that meteorology and photochemical process are the primary

326 factors (Feng et al., 2002;Feng et al., 2003;Wang et al., 2006;Feng et al., 2008;Fu et al., 2010;Fu et al.,

327 2013a;Fu et al., 2013b).

328 Overall, the annual net natural emission in China is 465.1 Mg Hg (Table 3), including 565.5 Mg yr$^{-1}$

329 from soil, 9.0 Mg yr$^{-1}$ from water body, and -100.4 Mg yr$^{-1}$ from the vegetation. The annual quantity of

330 emission from soil is comparable to the estimate (528 Mg yr$^{-1}$) based on the scale-up calculation using

331 measured air-soil fluxes (Fu et al., 2015a) that suggest emissions from cropland and grassland are the most

332 important contributor. Of the total Hg$^0$ emission estimated by the model, 50% is from shrubland, savanna

333 and grassland (C6-C11, 38% total landuse); 33% is from cropland (C12-C13, 22% total landuse); 9% is

334 from forest (C1-C5, 14% total landuse); and 8% is from other landuse types. Forest contributes to 28% of

335 Hg uptake by foliage; shrubland, savanna and grassland contribute to 38%; cropland contributes to 33%;

336 and other landuse types contribute to 1%.

337 Although soil Hg contents in forest ecosystems are 2-4 times higher than that in grassland and cropland,

338 total annual fluxes above the canopy (soil+foliage) of forest ecosystems are 1-6 times lower than the values

339 in other two types of landuses (Table 3). This highlights the importance of canopy cover in natural emission

340 process of Hg$^0$. It is noteworthy that the landuse data are based on the survey in 2000 (Ran et al., 2012).

341 From 2000 to 2013, the forested area in China increased from 14.0% to 21.6% (FAO, 2014), benefiting

342 from implementation of governmental Grain for Green Project and stricter natural forest protection actions.

343 Assuming that annual mean air-surface fluxes are at the same level as in this study, the total quantity of

344 natural Hg emission in 2013 is approximately 5% smaller than this estimate because of the increasing forest

345 coverage. Given the forest coverage is projected to be 24 to 26% during 2030-2050 (FAO, 2014), the

346 quantity of natural Hg emission in China would decrease by 9-10% compared to the estimated level of 2013.

347

## 348 3.3 Spatial distribution of natural Hg emission in China

349 The spatial distribution of annual air-foliage flux can be divided by the well-known geo-demographic

350 demarcation line, "Heihe-Tengchong Line" (Figure 6.1). The vegetation on the east side of the line is much

351 denser than on the west side of the line because of the higher annual precipitation (≥ 800 mm, Figure **S2**)

352 that leads to stronger Hg$^0$ uptake by vegetation (>90% of the grid cells have a flux below -1.0 ng m$^{-2}$ h$^{-1}$ on

353     the east side, compared to >90% of the grid cells has a flux above -0.5 ng m$^{-2}$ h$^{-1}$ on the west side). There is

354     an enhanced Hg deposition in South China (22˚N-27˚N, 105˚E-113˚E, Figure 6.1), with the fluxes ranging

355     -3.8 to -19.1 ng m$^{-2}$ h$^{-1}$. This can be explained by the elevated atmospheric Hg concentrations (2-10 ng m$^{-3}$)

356     and dense vegetation (i.e., high LAI, Figure **S3**) that enhance Hg uptake (Fu et al., 2015;Zhu, 2014).

357     Specifically, evergreen broadleaf forest has the highest LAI compared to other type of forests (Liu et al.,

358     2012) and shows enhanced Hg uptake (up to -4.5 ng m$^{-2}$ h$^{-1}$ mean flux). Although the direct measurement

359     of Hg deposition flux through vegetative uptake is still not presently feasible, the measured Hg input

360     through litterfall (Fu et al., 2015) suggested the rate of Hg uptake by foliage could be in the range of 4-12

361     ng m$^{-2}$ h$^{-1}$, comparable to the simulation results in this study.

362        Figure 6.2 shows the spatial distribution of annual air-soil fluxes. There are three high flux regions

363     (mean flux $\geq$ 10 ng m$^{-2}$ h$^{-1}$): cropland/grassland in South and Southwest China (mainly in Guangdong,

364     Guangxi, Guizhou, Yunnan, Chongqing and Sichuan provinces), cropland in North China (Heibei, Henan,

365     and Shangdong provinces), and grassland in North China (Inner Mongolia, Shanxi, and Shaanxi, and

366     Xinjiang provinces). Such elevated fluxes in the first two regions have been confirmed in field studies (Feng

367     et al., 2005;Wang et al., 2005;Wang et al., 2006;Fu et al., 2008;Sommar et al., 2015b). The high fluxes in

368     South and Southwest China are attributed to the elevated Hg concentration in soil (85% of grid cells has a

369     soil Hg content $\geq$100 ng g-1, Figure 1). Interestingly, soil Hg content is not the primary factor causing the

370     high fluxes in the other two regions (70% of grid cells has a soil Hg content $\leq$50 ng g$^{-1}$). Dry deposition of

371     PBM and/or GOM plausibly supply the reducible Hg in soil for gradual reduction and volatilization as Hg$^0$

372     (Sommar et al., 2015b). The relatively low LAI (Figure S3), strong solar irradiance and high soil

373     temperature (Figure **S4-S5**) during summer/autumn contribute to the high simulated emissions. The lower

374     simulated fluxes in desert regions compared to fluxes over grassland (Figure 6.2) are caused by the lower

375     fraction of reducible Hg in soils.

376        Since the soil Hg$^0$ flux is the primary source of natural Hg emission, the spatial distribution of the

377     natural Hg emission is strongly influenced by air-soil flux (Figure 7.1). There is a distinct seasonal variation

378     in the emission quantity: 8% in winter, 28% in spring, 51% in summer, and 13% in autumn (Figure 7.2-

379     7.5). Elevated fluxes mainly cluster in South and Southwest China during winter because of higher soil Hg

380  content (Figure 1), and relatively higher temperature and stronger irradiance. Highest correlation

381  coefficients are found between the flux and soil Hg concentration and soil bulk density (Table 4), suggesting

382  that the soil $Hg^0$ pool is a major factor influencing Hg emission in winter. From the cold to warm season,

383  fluxes gradually increase from low latitude to high latitude with the seasonal change of temperature and

384  solar radiation (Figure 7.2-7.4). Under the strong irradiance and temperatures in summer, >65% of the grid

385  cells in the domain has a flux above 10 ng $m^{-2}$ $h^{-1}$ and the effect of soil Hg content is relatively weaker

386  (Table 4). In autumn, higher flux occurs over the cropland of Central and North China, and over the regions

387  with high soil Hg content (Figure 7.6) because of the decreasing temperature and solar irradiance in the

388  south and the influence of soil Hg content in the north. Overall, 72% of natural Hg emission occurs from

389  May to September, with higher emission over grassland and cropland in North China in these months.

390      It is worth noting that parts of regions in South China (23˚N-31˚N, 110˚E-120˚E, mainly in Fujian,

391  Jiangxi, Hunan, Hubei, and Anhui provinces) and Northeast China (39˚N-51˚N, 130˚E-134˚E, mainly in

392  Liaoning, Jilin and Heilongjiang provinces) have relatively lower fluxes (-6.9~9.0 ng $m^{-2}$ $h^{-1}$) during

393  summer and autumn time (Figure 7.4-7.5). In addition to the impact from the intensive canopy cover in

394  forested area (Figure **S2**), agricultural activities in these regions also contribute to the smaller fluxes. Based

395  on Liu et al. (2013), 60% croplands in these regions are flooded for rice planting in summer and autumn.

396  Field-scale flux measurement using micrometeorological methods (i.e., aerodynamic gradient method)

397  suggest that a typical oilseeds-rice rotated cropland in Southwest China is a significant source during

398  oilseeds planting seasons with fluxes of 10.1-89.4 ng $m^{-2}$ $h^{-1}$; and a mild sink during rice planting seasons

399  with fluxes of -3.4 to -15.8 ng $m^{-2}$ $h^{-1}$ (Zhu, 2014). The model also successfully simulates such a pattern,

400  with simulated fluxes at 1.1-101.5 ng $m^{-2}$ $h^{-1}$ (Figure 7.2-7.3) during winter and earlier spring when

401  croplands are not flooded and at -3.5 to 1.5 ng $m^{-2}$ $h^{-1}$ during the rice growing season (Figure S6). Overall,

402  3.3 Mg $Hg^0$ is predicted to deposit into rice paddies during the rice growing season, with 56% of the

403  deposition occurring in summer, 41% in autumn, and 3% in late spring.

404

405  **3.4 Verification of model estimates**

406      For the first time, the simulated natural Hg emission in China is verified against field observational

407    data in this study. The dataset of Hg deposition through litterfall is utilized for verifying the simulated air-

408    foliage fluxes because of two reasons: (1) it has been shown that Hg deposition through litterfall dominates

409    dry deposition (≥70%) in forests of China (Fu et al., 2015); and the annual Hg deposition through litterfall

410    has been used as a surrogate to constrain air-foliage fluxes in forest ecosystems (Risch et al., 2012;Zhang

411    et al., 2012a), and (2) the litterfall data in China comprehensively include different forest types compared

412    to the limited locations where air-foliage flux data are available. For verifying the exchange fluxes over

413    water and soil surfaces, the flux measurements over forest soil, grassland, cropland and water body in China

414    (Table **S2**) are utilized.

415        To estimate the annual Hg deposition through litterfall in the study domain, Monte Carlo simulation

416    (described in details in SI) is applied for constructing the probability distribution of the Hg deposition

417    through litterfall using litter biomass production and litterfall Hg concentration in China reported in peer-

418    reviewed literature (Figure 8). The sampling locations include 20 sites in Tibetan Plateau, 27 sites for

419    evergreen forests, and 12 sites for deciduous forests. The quality-assured data of litter biomass production

420    (number of replicates ≥ 3, collector size = 1 $m^2$) are obtained from the China National Knowledge

421    Infrastructure (CNKI). This dataset includes the measurements at 5 sites in Tibetan Plateau, 277 sites for

422    evergreen forests, 74 sites for deciduous forests, and 61 sites for mixed forests.

423        Figure S7 shows the observed Hg concentrations in litter. The Hg concentration for evergreen forest

424    ranges from 17 to 120 ng $g^{-1}$ with a mean of 52±26 ng $g^{-1}$. For deciduous forest, the range is 21-62 ng $g^{-1}$

425    with a mean of 38±12 ng $g^{-1}$. The difference between the concentrations observed in evergreen forests and

426    in deciduous forests is significant (paired *t* test, $p < 0.05$). The Hg concentration in litter for deciduous forest

427    in China is comparable to the values reported for the same forest type in Europe and North America ($p =$

428    0.101). Hg deposition through litterfall in evergreen broadleaf forest (C2, refer to Table 3 for the landuse

429    type) ranges from 26 to 72 μg $m^{-2}$ $y^{-1}$ (n=5 sites) with a mean of 43±27 μg $m^{-2}$ $y^{-1}$ (Fu et al., 2015;Ma et al.,

430    2015;Wang et al., 2009), consistent with the Hg deposition estimated by Monte Carlo simulation

431    (mean=37±19 μg $m^{-2}$ $y^{-1}$; 95% confidence interval is 4-89 μg $m^{-2}$ $y^{-1}$). The model-estimated Hg deposition

432    for C1, C3, C4, and C5 is 22±10, 15±7, 16±11, and 17±8 μg $m^{-2}$ $y^{-1}$, respectively.

433        The measured air-soil flux (Table **S2**) ranges from -1.4 to 20.7 ng $m^{-2}$ $h^{-1}$ over forest soil (n=19; mean=

434  $6.1\pm5.1$ ng m$^{-2}$ h$^{-1}$), from -18.7 to 114 ng m$^{-2}$ h$^{-1}$ over grassland (n=14; mean= $26\pm36$ ng m$^{-2}$ h$^{-1}$), from -4.1

435  to 135 ng m$^{-2}$ h$^{-1}$ over cropland (n=33; mean= $21.3\pm36.7$ ng m$^{-2}$ h$^{-1}$). For water body (n=51), the flux range

436  is 0-43.8 ng m$^{-2}$ h$^{-1}$ with a mean of $4.6\pm6.6$ ng m$^{-2}$ h$^{-1}$ (Table **S2**). The mean flux from May to October is

437  substantially higher than those from November to April: 3.3 times for water surface (p=0.004), 3.2 times

438  higher for forest soil (p=0.08), and 1.4 times for cropland (p=0.50). A reverse trend is found for grassland,

439  which has higher mean flux in cold seasons (50% higher, p=0.36). More measurements in grassland where

440  few data exist will greatly improve the accuracy of the current estimate.

441  Figures **S8**, **S9** and 8.1 compare the model estimates to the mean and variability level predicted by

442  Monte Carlo simulation using field data. The annual Hg uptake simulated by the bidirectional exchange

443  model is not significantly different from the field observations (p>0.05, t-test) and the spatial patters are

444  similar (Figure **S8**) in coniferous forest ecosystems, demonstrating the model capability for simulating the

445  air-foliage flux. However, the bidirectional exchange model did not capture the spatial distribution of air-

446  foliage flux in broadleaf forest ecosystems (particularly in evergreen broadleaf forest, Figure **S9**). One

447  possible explanation is that the resistance terms obtained from temperate/boreal forests (Zhang et al., 2012b)

448  may not appropriately represent the value in evergreen broadleaf forests. Filed measurements suggests that

449  the leaf stomatal conductance of broadleaf is usually higher than the value of needleleaf (Wang et al.,

450  2015;Ishida et al., 2006;Sobrado, 1991;Eamus, 1999), leading to a larger air-foliage Hg$^0$ exchange

451  (Graydon et al., 2006). Further studies on the Hg transport and chemical reactions at the air-foliage interface

452  in evergreen broadleaf forests will help constrain the model.

453  Figure 8.2 shows the scatter plot of the measured and model-predicted fluxed over soil and water

454  ($R^2$=0.73). Modeling results for over water surfaces and soil under forest canopy also agree with filed data

455  (Figure 8.3-8.4). The model results somewhat underestimates the high fluxes ($\geq$ 30 ng m$^{-2}$ h$^{-1}$, Figure **S9.2**)

456  measured over grassland and cropland (Figure 8.4), which be attributed to several possible reasons. One is

457  the bias caused by the comparatively coarser spatial resolution (36 km) of meteorological parameters and

458  soil properties that limit the reproduction of the instantaneously measured fluxes at observational sites. In

459  addition, the limited mechanistic understanding on the re-emission process after Hg dry deposition (Gustin

460  et al., 2015;Lindberg et al., 2007;Gustin et al., 2008b;Ariya et al., 2015) complicates model

461 parameterization. Finally, the uncertainties caused by flux quantification methodology (Lin et al., 2012;Zhu

462 et al., 2015b, c) and the typically short campaign periods (mostly ranging from several days to a couple of

463 weeks) could biased the measurement data (Feng et al., 2005;Fu et al., 2008;Fu et al., 2012;Fu et al.,

464 2015;Zhu et al., 2015b, c). Improvement on flux methods and extended campaign periods at more study

465 sites for cropland/grassland will help constrain the model estimates.

466

467 **3.5 Comparison with earlier estimates and implications on Hg emission outflow in China**

468      Figures **S10** and **S11** show the gridded natural Hg emission in the East Asian Domain reported by

469 Shetty et al. (2008) and Wang et al. (2014a), which have two distinct differences compared to the model

470 estimate in this study. One is the role of vegetation in natural Hg emission, the other is spatial distribution

471 of the emission. Vegetation is clearly an important sink of $Hg^0$ with the mechanistic model algorithms

472 implemented in this study; and the shading of vegetation suppress Hg evasion from soil under canopy. In

473 contrast, vegetation is considered a major source, accounting for 76% of total emissions in Shetty et al.

474 (2008) because the model treats Hg evasion as an evapotranspiration process that transports Hg from root

475 zone through vascular tissues in foliage (Gbor et al., 2007;Shetty et al., 2008). Recent experimental

476 evidence using stable Hg isotope tracers points to exclusion of this pathway for cereal plants (Cui et al.,

477 2014). In addition, Hg isotopic signatures observed in air and leaf samples (Demers et al., 2013;Yin et al.,

478 2013) and during air-foliage exchange process (Graydon et al., 2006;Gustin et al., 2008a) indicate uptake

479 of atmospheric Hg by foliage, pointing to vegetation as a $Hg^0$ sink. In contrast to the spatial distribution of

480 the emission in this study, the earlier $Hg^0$ emission estimates occur mainly in the regions on the east side of

481 the "Heihe-Tengchong Line" (Shetty et al., 2008;Wang et al., 2014a), due to the spatial distribution of

482 vegetation (Shetty et al. (2008) or soil Hg content (Wang et al. (2014a).

483     This study advances upon the earlier estimates (Shetty et al., 2008;Wang et al., 2014a) in three areas.

484 Firstly, the recent soil survey data including soil Hg content and other soil characteristics is a major

485 advantage in this study. The soil Hg data applied in Shetty et al. (2008) is outdated with a coarse spatial

486 resolution; while the data in Wang et al. (2014a) is based on the output of the global terrestrial Hg model in

487 GEOS-Chem, calculated from Hg/C ratios. Secondly, the mechanistic model scheme better describe the air-

488    surface exchange process compared the regression and evapotranspiration in the earlier studies. Finally, the

489    model estimates are verified against the field flux data with generally good agreement, which has not been

490    attempted in earlier works.

491        Although the total quantity of annual natural emission estimated in this study is comparable to earlier

492    estimates (400-600 Mg yr$^{-1}$) by Shetty et al. (2008) and Wang et al. (2014a) , the distinct spatial distribution

493    of natural emissions simulated in this study may alter the current understanding of Hg emission outflow

494    from China assessed by Lin et al. (2010b). The outflow of Hg emissions in China is mainly driven by the

495    prevailing west-wind drift (Lin et al., 2010b;Chen et al., 2014). The predominant natural Hg emission in

496    the west side of model domain results in a longer residence time of evaded Hg, which can be more readily

497    oxidized and deposited within the domain. Furthermore, the dense vegetation in the east side of the domain

498    can also help capture the nature Hg$^0$ emission, potentially leading to substantially larger domestic deposition

499    and smaller quantity of outflow compared to the estimates by Lin et al. (2010). We are presently to reassess

500    the emission outflow using a regional chemical transport model (e.g., CMAQ-Hg) and a similar mass

501    balance approach by Lin et al. (2010); and will report the model results in a future paper.

502

503    **4. Conclusions**

504        Using a mechanistic model incorporating the present state of understanding in Hg transformation in

505    soils and on foliage surface with up-to-date datasets of soil characteristics and landuse changes, the natural

506    emission of Hg$^0$ vapor in China is estimated to be 465.1 Mg yr$^{-1}$, including 565.5 Mg yr$^{-1}$ of emission from

507    soils, 9.0 Mg yr$^{-1}$ of emission from water bodies, and -100.4 Mg yr$^{-1}$ deposition (uptake) by vegetation. The

508    air-surface exchange is strongly dependent on landuse and meteorology, with 9% of net emission from

509    forest ecosystems, 50% from shrubland, savanna and grassland, 33% from cropland, and 8% from other

510    landuses. Given the large agricultural land area in China, farming activities play an important role on the

511    air-surface exchange. Particularly, rice fields shift from a net sink (3.3 Mg uptake) during the growing

512    season in rice paddy to a net source during the season when the farmland is not flooded. The estimated

513    natural Hg$^0$ emission in this study yields similar Hg$^0$ evasion quantity but exhibits contrasting spatial

514    distribution compared to the estimate by Shetty et al. (2008). The difference in the spatial patterns may alter

515    the current understanding of Hg emission outflow from China as reported by Lin et al. (2010b) because of

516 a substantial amount of natural $Hg^0$ emission occurs in West China, which requires further assessment.

517 For future model improvement, studies focusing on fundamental understanding of $Hg^{II}$ reduction in

518 soil (especially the role of soil organic matter, contribution of photochemical and non-chemical pathways,

519 and radiation transfer in soil) and air-vegetation exchange mechanisms are needed. Continuous updates on

520 the data of soil characteristics and Hg content is also essential. More field data for model performance

521 evaluation is also important for constraining the model. In particular, data of air-foliage flux, and air-soil

522 flux over cropland and grassland in the remote regions of North China is valuable for model calibration.

523

524 **Acknowledgements**

525 This work was funded by National "973" Program of China (2013CB430003), and State Key Laboratory

526 of Environmental Geochemistry, IGCAS. The funding support is gratefully acknowledged.

527

528 **References**

529 Ariya, P. A., Amyot, M., Dastoor, A., Deeds, D., Feinberg, A., Kos, G., Poulain, A., Ryjkov, A., Semeniuk, K., Subir, M.,

530 and Toyota, K.: Mercury Physicochemical and Biogeochemical Transformation in the Atmosphere and at Atmospheric

531 Interfaces: A Review and Future Directions, Chem Rev, 115, 3760-3802, 2015.

532 Bash, J. O., Miller, D. R., Meyer, T. H., and Bresnahan, P. A.: Northeast United States and Southeast Canada natural

533 mercury emissions estimated with a surface emission model, Atmos Environ, 38, 5683-5692, 2004.

534 Bash, J. O., Bresnahan, P., and Miller, D. R.: Dynamic surface interface exchanges of mercury: A review and

535 compartmentalized modeling framework, Journal of Applied Meteorology and Climatology, 46, 1606-1618,

536 10.1175/jam2553.1, 2007.

537 Bash, J. O.: Description and initial simulation of a dynamic bidirectional air-surface exchange model for mercury in

538 Community Multiscale Air Quality (CMAQ) model, J Geophys Res-Atmos, 115, 2010.

539 Carpi, A., and Lindberg, S. E.: Application of a Teflon (TM) dynamic flux chamber for quantifying soil mercury flux:

540 Tests and results over background soil, Atmos Environ, 32, 873-882, 1998.

541 Chen, L., Wang, H. H., Liu, J. F., Tong, Y. D., Ou, L. B., Zhang, W., Hu, D., Chen, C., and Wang, X. J.: Intercontinental

542 transport and deposition patterns of atmospheric mercury from anthropogenic emissions, Atmos Chem Phys, 14,

543 10163-10176, 2014.

544 Choi, H. D., and Holsen, T. M.: Gaseous mercury fluxes from the forest floor of the Adirondacks, Environmental

545 Pollution, 157, 592-600, 2009.

546 Ciani, A., Goss, K. U., and Schwarzenbach, R. P.: Light penetration in soil and particulate minerals, Eur J Soil Sci, 56,

547 561-574, 2005.

548 Cui, L., Feng, X., Lin, C.-J., Wang, X., Meng, B., Wang, X., and Wang, H.: Accumulation and translocation of [198]Hg in

549 four crop species, Environ Toxicol Chem, 33, 334-340, 2014.

550 Demers, J. D., Blum, J. D., and Zak, D. R.: Mercury isotopes in a forested ecosystem: Implications for air-surface

551 exchange dynamics and the global mercury cycle, Global Biogeochemical Cycles, 27, 222-238, 10.1002/gbc.20021,

552 2013.

553  Ericksen, J., and Gustin, M. S.: Air-surface exchange of mercury with soils amended with ash materials, J Air Waste
554  Manage, 56, 977-992, 2006.
555  Ericksen, J. A., Gustin, M. S., Xin, M., Weisberg, P. J., and Fernandez, G. C. J.: Air-soil exchange of mercury from
556  background soils in the United States, Sci Total Environ, 366, 851-863, 2006.
557  Fain, X., Grangeon, S., Bahlmann, E., Fritsche, J., Obrist, D., Dommergue, A., Ferrari, C. P., Cairns, W., Ebinghaus, R.,
558  Barbante, C., Cescon, P., and Boutron, C.: Diurnal production of gaseous mercury in the alpine snowpack before
559  snowmelt, J Geophys Res-Atmos, 112, 2007.
560  FAO: State of the World's Forests 2014, FOOD AND AGRICULTURE ORGANIZATION OF THE UNITED NATIONS, Rome,
561  93-100, 2014.
562  Feng, X., Qiu, G., Wang, S., and Shang, L.: Distribution and speciation of mercury in surface waters in mercury mining
563  areas in Wanshan, Southwestern China, J Phys Iv, 107, 455-458, 2003.
564  Feng, X. B., Sommar, J., Gardfeldt, K., and Lindqvist, O.: Exchange flux of total gaseous mercury between air and
565  natural water surfaces in summer season, Sci China Ser D, 45, 211-220, 2002.
566  Feng, X. B., Wang, S. F., Qiu, G. A., Hou, Y. M., and Tang, S. L.: Total gaseous mercury emissions from soil in Guiyang,
567  Guizhou, China, J Geophys Res-Atmos, 110, 2005.
568  Feng, X. B., Wang, S. F., Qiu, G. G., He, T. R., Li, G. H., Li, Z. G., and Shang, L. H.: Total gaseous mercury exchange
569  between water and air during cloudy weather conditions over Hongfeng Reservoir, Guizhou, China, J Geophys Res-
570  Atmos, 113, 2008.
571  Fritsche, J., Wohlfahrt, G., Ammann, C., Zeeman, M., Hammerle, A., Obrist, D., and Alewell, C.: Summertime
572  elemental mercury exchange of temperate grasslands on an ecosystem-scale, Atmospheric Chemistry and Physics, 8,
573  2008.
574  Fu, X. W., Feng, X. B., and Wang, S. F.: Exchange fluxes of Hg between surfaces and atmosphere in the eastern flank
575  of Mount Gongga, Sichuan province, southwestern China, Journal of Geophysical Research-Atmospheres, 113, 2008.
576  Fu, X. W., Feng, X. B., Zhang, G., Xu, W. H., Li, X. D., Yao, H., Liang, P., Li, J., Sommar, J., Yin, R. S., and Liu, N.: Mercury
577  in the marine boundary layer and seawater of the South China Sea: Concentrations, sea/air flux, and implication for
578  land outflow, J Geophys Res-Atmos, 115, 2010.
579  Fu, X. W., Feng, X. B., Zhang, H., Yu, B., and Chen, L. G.: Mercury emissions from natural surfaces highly impacted by
580  human activities in Guangzhou province, South China, Atmos Environ, 54, 185-193, 2012.
581  Fu, X. W., Feng, X. B., Guo, Y. N., Meng, B., Yin, R. S., and Yao, H.: Distribution and production of reactive mercury and
582  dissolved gaseous mercury in surface waters and water/air mercury flux in reservoirs on Wujiang River, Southwest
583  China, J Geophys Res-Atmos, 118, 3905-3917, 2013a.
584  Fu, X. W., Feng, X. B., Yin, R. S., and Zhang, H.: Diurnal variations of total mercury, reactive mercury, and dissolved
585  gaseous mercury concentrations and water/air mercury flux in warm and cold seasons from freshwaters of
586  southwestern China, Environ Toxicol Chem, 32, 2256-2265, 2013b.
587  Fu, X. W., Zhang, H., Wang, X., Yu, B., Lin, C.-J., and Feng, X. B.: Observations of atmospheric mercury in China: a
588  critical review, Atmos. Chem. Phys. Discuss., 11925-11983, doi:10.5194/acpd-15-11925-2015, 2015.
589  Gbor, P. K., Wen, D. Y., Meng, F., Yang, F. Q., Zhang, B. N., and Sloan, J. J.: Improved model for mercury emission,
590  transport and deposition, Atmospheric Environment, 40, 973-983, DOI 10.1016/j.atmosenv.2005.10.040, 2006.
591  Gbor, P. K., Wen, D. Y., Meng, F., Yang, F. Q., and Sloan, J. J.: Modeling of mercury emission, transport and deposition
592  in North America, Atmospheric Environment, 41, 1135-1149, DOI 10.1016/j.atmosenv.2006.10.005, 2007.
593  Graydon, J. A., St Louis, V. L., Lindberg, S. E., Hintelmann, H., and Krabbenhoft, D. P.: Investigation of mercury exchange

594    between forest canopy vegetation and the atmosphere using a new dynamic chamber, Environ Sci Technol, 40, 4680-
595    4688, 2006.

596    Gustin, M. S., Lindberg, S. E., and Weisberg, P. J.: An update on the natural sources and sinks of atmospheric mercury,
597    Appl Geochem, 23, 482-493, 2008a.

598    Gustin, M. S., Lindberg, S. E., and Weisberg, P. J.: An update on the natural sources and sinks of atmospheric mercury,
599    Applied Geochemistry, 23, 10.1016/j.apgeochem.2007.12.010, 2008b.

600    Gustin, M. S., Amos, H. M., Huang, J., Miller, M. B., and Heidecorn, K.: Measuring and modeling mercury in the
601    atmosphere: a critical review, Atmos Chem Phys, 15, 5697-5713, 2015.

602    He, F., Zheng, W., Liang, L. Y., and Gu, B. H.: Mercury photolytic transformation affected by low-molecular-weight
603    natural organics in water, Sci Total Environ, 416, 429-435, 2012.

604    Hebert, V. R., and Miller, G. C.: Depth dependence of direct and indirect photolysis on soil surfaces, J. Agric. Food
605    Chem., 38, 913-918, DOI: 10.1021/jf00093a069, 1990.

606    Hood, A., Gutjahr, C. C. M., and Heacock, R. L.: Organic Metamorphism and the Generation of Petroleum, AAPG
607    BULLETIN, 59, 986-996, 1975.

608    Horowitz, H. M., Jacob, D. J., Amos, H. M., Streets, D. G., and Sunderland, E. M.: Historical Mercury Releases from
609    Commercial Products: Global Environmental Implications, Environ Sci Technol, 48, 10242-10250, 2014.

610    Jaffe, D., Prestbo, E., Swartzendruber, P., Weiss-Penzias, P., Kato, S., Takami, A., Hatakeyama, S., and Kajii, Y.: Export
611    of atmospheric mercury from Asia, Atmos Environ, 39, 3029-3038, 2005.

612    Kissinger, H. E.: Reaction Kinetics in Differential Thermal Analysis, The Journal of Physical Chemistry 29, 1702-1706,
613    DOI: 10.1021/ac60131a045, 1957.

614    Kuiken, T., Gustin, M., Zhang, H., Lindberg, S., and Sedinger, B.: Mercury emission from terrestrial background
615    surfaces in the eastern USA. II: Air/surface exchange of mercury within forests from South Carolina to New England,
616    Appl Geochem, 23, 356-368, 2008a.

617    Kuiken, T., Zhang, H., Gustin, M., and Lindberg, S.: Mercury emission from terrestrial background surfaces in the
618    eastern USA. Part I: Air/surface exchange of mercury within a southeastern deciduous forest (Tennessee) over one
619    year, Appl Geochem, 23, 345-355, 2008b.

620    Laacouri, A., Nater, E. A., and Kolka, R. K.: Distribution and Uptake Dynamics of Mercury in Leaves of Common
621    Deciduous Tree Species in Minnesota, USA, Environ Sci Technol, 47, 10462-10470, 2013.

622    Lalonde, J. D., Amyot, M., Doyon, M. R., and Auclair, J. C.: Photo-induced Hg(II) reduction in snow from the remote
623    and temperate Experimental Lakes Area (Ontario, Canada), Journal of Geophysical Research-Atmospheres, 108, Artn
624    4200
625    Doi 10.1029/2001jd001534, 2003.

626    Lee, S. Z., Chang, L., Chen, C. M., Tsai, Y. I., and Liu, M. C.: Predicting soil-water partition coefficients for Hg(II) from
627    soil properties, Water Sci Technol, 43, 187-196, 2001.

628    Li, M., Xi, X. H., Xiao, G. Y., Cheng, H. X., Yang, Z. F., Zhou, G. H., Ye, J. Y., and Li, Z. H.: National multi-purpose regional
629    geochemical survey in China, J Geochem Explor, 139, 21-30, 2014.

630    Lin, C.-J., Gustin, M. S., Singhasuk, P., Eckley, C., and Miller, M.: Empirical Models for Estimating Mercury Flux from
631    Soils, Environmental Science & Technology, 44, 8522-8528, 10.1021/es1021735, 2010a.

632    Lin, C. J., Lindberg, S. E., Ho, T. C., and Jang, C.: Development of a processor in BEIS3 for estimating vegetative mercury
633    emission in the continental United States, Atmos Environ, 39, 7529-7540, 2005.

634    Lin, C. J., Pan, L., Streets, D. G., Shetty, S. K., Jang, C., Feng, X., Chu, H. W., and Ho, T. C.: Estimating mercury emission

635    outflow from East Asia using CMAQ-Hg, Atmos Chem Phys, 10, 1853-1864, 2010b.

636    Lin, C. J., Zhu, W., Li, X. C., Feng, X. B., Sommar, J., and Shang, L. H.: Novel Dynamic Flux Chamber for Measuring Air-

637    Surface Exchange of Hg-o from Soils, Environmental Science & Technology, 46, 8910-8920, Doi 10.1021/Es3012386,

638    2012.

639    Lindberg, S. E., Zhang, H., Gustin, M., Vette, A., Marsik, F., Owens, J., Casimir, A., Ebinghaus, R., Edwards, G., Fitzgerald,

640    C., Kemp, J., Kock, H. H., London, J., Majewski, M., Poissant, L., Pilote, M., Rasmussen, P., Schaedlich, F., Schneeberger,

641    D., Sommar, J., Turner, R., Wallschlager, D., and Xiao, Z.: Increases in mercury emissions from desert soils in response

642    to rainfall and irrigation, J Geophys Res-Atmos, 104, 21879-21888, 1999.

643    Lindberg, S. E., Dong, W. J., and Meyers, T.: Transpiration of gaseous elemental mercury through vegetation in a

644    subtropical wetland in Florida, Atmos Environ, 36, 5207-5219, 2002.

645    Lindberg, S. E., Bullock, R., Ebinghaus, R., Engstrom, D., Feng, X. B., Fitzgerald, W., Pirrone, N., Prestbo, E., and

646    Seigneur, C.: A synthesis of progress and uncertainties in attributing the sources of mercury in deposition, Ambio, 36,

647    19-32, 2007.

648    Liu, L., Xu, X. L., Zhuang, D. F., Chen, X., and Li, S.: Changes in the Potential Multiple Cropping System in Response to

649    Climate Change in China from 1960-2010, Plos One, 8, 2013.

650    Liu, Y. B., Ju, W. M., Chen, J. M., Zhu, G. L., Xing, B. L., Zhu, J. F., and He, M. Z.: Spatial and temporal variations of forest

651    LAI in China during 2000-2010, Chinese Science Bulletin, 57, 2846-2856, 2012.

652    Lyon, B. F., Ambrose, R., Rice, G., and Maxwell, C. J.: Calculation of soil-water and benthic sediment partition

653    coefficients for mercury, Chemosphere, 35, 791-808, 1997.

654    Ma, M., Wang, D. Y., Du, h. X., Z, Z., and W, S. Q.: Atmospheric mercury deposition and its contribution of the regional

655    atmospheric transport to mercury pollution at a national forest nature reserve, southwest China, Environ Sci Pollut

656    R, DOI 10.1007/s11356-015-5152-9, 2015.

657    Mann, E. A., Mallory, M. L., Ziegler, S. E., Avery, T. S., Tordon, R., and O'Driscoll, N. J.: Photoreducible Mercury Loss

658    from Arctic Snow Is Influenced by Temperature and Snow Age, Environmental Science & Technology, 49, 12120-12126,

659    2015.

660    Mauclair, C., Layshock, J., and Carpi, A.: Quantifying the effect of humic matter on the emission of mercury from

661    artificial soil surfaces, Appl Geochem, 23, 594-601, 2008.

662    Maxwell, J. A., Holsen, T. M., and Mondal, S.: Gaseous Elemental Mercury (GEM) Emissions from Snow Surfaces in

663    Northern New York, Plos One, 8, 2013.

664    Moan, J.: 7 Visible Light and UV Radiation, Radiation, 69, 2001.

665    Moore, C., and Carpi, A.: Mechanisms of the emission of mercury from soil: Role of UV radiation, J Geophys Res-

666    Atmos, 110, 2005.

667    Moore, C. W., and Castro, M. S.: Investigation of factors affecting gaseous mercury concentrations in soils, Science of

668    the Total Environment, 419, 136-143, 2012.

669    O'Driscoll, N. J., Siciliano, S. D., Lean, D. R. S., and Amyot, M.: Gross photoreduction kinetics of mercury in temperate

670    freshwater lakes and rivers: Application to a general model of DGM dynamics, Environ Sci Technol, 40, 837-843, 2006.

671    Obrist, D., Pokharel, A. K., and Moore, C.: Vertical Profile Measurements of Soil Air Suggest Immobilization of Gaseous

672    Elemental Mercury in Mineral Soil, Environ Sci Technol, 48, 2242-2252, 2014.

673    Pacyna, J. M., Travnikov, O., De Simone, F., Hedgecock, I. M., Sundseth, K., Pacyna, E. G., Steenhuisen, F., Pirrone, N.,

674    Munthe, J., and Kindbom, K.: Current and future levels of mercury atmospheric pollution on global scale, Atmos.

675    Chem. Phys. Discuss., 2016, 1-35, 10.5194/acp-2016-370, 2016.

676    Pannu, R.: QUANTIFYING MERCURY REDUCTION KINETICS IN SOILS, Degree of Doctor of Philosophy, Department of

677    Soil Science, University of Saskatchewan, 156 pp., 2012.

678    Pannu, R., Siciliano, S. D., and O'Driscoll, N. J.: Quantifying the effects of soil temperature, moisture and sterilization

679    on elemental mercury formation in boreal soils, Environmental Pollution, 193, 138-146, 2014.

680    Pirrone, N., Cinnirella, S., Feng, X., Finkelman, R. B., Friedli, H. R., Leaner, J., Mason, R., Mukherjee, A. B., Stracher, G.

681    B., Streets, D. G., and Telmer, K.: Global mercury emissions to the atmosphere from anthropogenic and natural

682    sources, Atmos Chem Phys, 10, 5951-5964, 2010.

683    Poissant, L., Pilote, M., Yumvihoze, E., and Lean, D.: Mercury concentrations and foliage/atmosphere fluxes in a maple

684    forest ecosystem in Quebec, Canada, Journal of Geophysical Research-Atmospheres, 113, 10.1029/2007jd009510,

685    2008.

686    Quinones, J. L., and Carpi, A.: An Investigation of the Kinetic Processes Influencing Mercury Emissions from Sand and

687    Soil Samples of Varying Thickness, Journal of Environmental Quality, 40, 647-652, 10.2134/jeq2010.0327, 2011.

688    Qureshi, A., O'Driscoll, N. J., MacLeod, M., Neuhold, Y. M., and Hungerbuhler, K.: Photoreactions of Mercury in

689    Surface Ocean Water: Gross Reaction Kinetics and Possible Pathways, Environ Sci Technol, 44, 644-649, 2010.

690    Qureshi, A., MacLeod, M., and Hungerbuhler, K.: Quantifying uncertainties in the global mass balance of mercury,

691    Global Biogeochemical Cycles, 25, GB4012, Gb4012, 10.1029/2011gb004068, 2011.

692    Ran, Y. H., Li, X., Lu, L., and Li, Z. Y.: Large-scale land cover mapping with the integration of multi-source information

693    based on the Dempster-Shafer theory, Int J Geogr Inf Sci, 26, 169-191, 2012.

694    Risch, M. R., DeWild, J. F., Krabbenhoft, D. P., Kolka, R. K., and Zhang, L. M.: Litterfall mercury dry deposition in the

695    eastern USA, Environ Pollut, 161, 284-290, 2012.

696    Sauve, S., Hendershot, W., and Allen, H. E.: Solid-solution partitioning of metals in contaminated soils: Dependence

697    on pH, total metal burden, and organic matter, Environmental Science & Technology, 34, 1125-1131, 2000.

698    Scholtz, M. T., Van Heyst, B. J., and Schroeder, W.: Modelling of mercury emissions from background soils, Science of

699    the Total Environment, 304, 185-207, 10.1016/s0048-9697(02)00568-5, 2003.

700    Selin, N. E., Jacob, D. J., Yantosca, R. M., Strode, S., Jaegle, L., and Sunderland, E. M.: Global 3-D land-ocean-

701    atmosphere model for mercury: Present-day versus preindustrial cycles and anthropogenic enrichment factors for

702    deposition (vol 22, artn no GB3099, 2008), Global Biogeochem Cy, 22, 2008.

703    Selin, N. E.: Global Biogeochemical Cycling of Mercury: A Review, Annu Rev Env Resour, 34, 43-63, 2009.

704    Shangguan, W., Dai, Y., Liu, B., Zhu, A., Duan, Q., Wu, L., Ji, D., Ye, A., Yuan, H., Zhang, Q., Chen, D., Chen, M., Chu, J.,

705    Dou, Y., Guo, J., Li, H., Li, J., Liang, L., Liang, X., Liu, H., Liu, S., Miao, C., and Zhang, Y.: A China data set of soil properties

706    for land surface modeling, J Adv Model Earth Sy, 5, 212-224, 10.1002/jame.20026, 2013.

707    Shetty, S. K., Lin, C. J., Streets, D. G., and Jang, C.: Model estimate of mercury emission from natural sources in East

708    Asia, Atmos Environ, 42, 8674-8685, 2008.

709    Si, L., and Ariya, P. A.: Aqueous photoreduction of oxidized mercury species in presence of selected alkanethiols,

710    Chemosphere, 84, 1079-1084, 2011.

711    Si, L., and Ariya, P. A.: Photochemical reactions of divalent mercury with thioglycolic acid: Formation of mercuric

712    sulfide particles, Chemosphere, 119, 467-472, 2015.

713    Smith-Downey, N. V., Sunderland, E. M., and Jacob, D. J.: Anthropogenic impacts on global storage and emissions of

714    mercury from terrestrial soils: Insights from a new global model, Journal of Geophysical Research-Biogeosciences,

715    115, Artn G03008

716    Doi 10.1029/2009jg001124, 2010.

717     Sommar, J., Zhu, W., Lin, C. J., and Feng, X. B.: Field Approaches to Measure Hg Exchange Between Natural Surfaces
718     and the Atmosphere A Review, Critical Reviews in Environmental Science and Technology, 43, 1657-1739, Doi
719     10.1080/10643389.2012.671733, 2013a.

720     Sommar, J., Zhu, W., Shang, L. H., Feng, X. B., and Lin, C. J.: A whole-air relaxed eddy accumulation measurement
721     system for sampling vertical vapour exchange of elemental mercury, Tellus B, 65, 2013b.

722     Sommar, J., Zhu, W., Shang, L., Lin, C. J., and Feng, X. B.: Seasonal variations in metallic mercury (Hg0) vapor exchange
723     over biannual wheat – corn rotation cropland in the North China Plain, Biogeosciences Discuss., 12, 16105-
724     16158, 2015a.

725     Sommar, J., Zhu, W., Shang, L., Lin, C. J., and Feng, X. B.: Seasonal variations in metallic mercury (Hg0) vapor exchange
726     over biannual wheat - corn rotation cropland in the North China Plain, Biogeosciences Discussions, 12, 16105-16158,
727     2015b.

728     Song, S., Selin, N. E., Soerensen, A. L., Angot, H., Artz, R., Brooks, S., Brunke, E. G., Conley, G., Dommergue, A.,
729     Ebinghaus, R., Holsen, T. M., Jaffe, D. A., Kang, S., Kelley, P., Luke, W. T., Magand, O., Marumoto, K., Pfaffhuber, K. A.,
730     Ren, X., Sheu, G. R., Slemr, F., Warneke, T., Weigelt, A., Weiss-Penzias, P., Wip, D. C., and Zhang, Q.: Top-down
731     constraints on atmospheric mercury emissions and implications for global biogeochemical cycling, Atmos Chem Phys,
732     15, 7103-7125, 2015.

733     Streets, D. G., Zhang, Q., and Wu, Y.: Projections of Global Mercury Emissions in 2050, Environ Sci Technol, 43, 2983-
734     2988, 2009.

735     Streets, D. G., Devane, M. K., Lu, Z. F., Bond, T. C., Sunderland, E. M., and Jacob, D. J.: All-Time Releases of Mercury
736     to the Atmosphere from Human Activities, Environ Sci Technol, 45, 10485-10491, 2011.

737     Strode, S. A., Jaegle, L., Jaffe, D. A., Swartzendruber, P. C., Selin, N. E., Holmes, C., and Yantosca, R. M.: Trans-Pacific
738     transport of mercury, J Geophys Res-Atmos, 113, 2008.

739     Wang, D. Y., He, L., Shi, X. J., Wei, S. Q., and Feng, X. B.: Release flux of mercury from different environmental surfaces
740     in Chongqing, China, Chemosphere, 64, 1845-1854, 2006.

741     Wang, S., Zhang, L., Wang, L., Wu, Q., Wang, F., and Hao, J.: A review of atmospheric mercury emissions, pollution
742     and control in China, Frontiers of Environmental Science & Engineering, 8, 631-649, 10.1007/s11783-014-0673-x,
743     2014a.

744     Wang, S. F., Feng, X. B., Qiu, G. L., Wei, Z. Q., and Xiao, T. F.: Mercury emission to atmosphere from Lanmuchang Hg-
745     Tl mining area, Southwestern Guizhou, China, Atmos Environ, 39, 7459-7473, 2005.

746     Wang, X., Lin, C. J., and Feng, X.: Sensitivity analysis of an updated bidirectional air-surface exchange model for
747     elemental mercury vapor, Atmos Chem Phys, 14, 6273-6287, 2014b.

748     Wang, Z. W., Zhang, X. S., Xiao, J. S., Zhijia, C., and Yu, P. Z.: Mercury fluxes and pools in three subtropical forested
749     catchments, southwest China, Environ Pollut, 157, 801-808, 2009.

750     Wright, L. P., and Zhang, L. M.: An approach estimating bidirectional air-surface exchange for gaseous elemental
751     mercury at AMNet sites, J Adv Model Earth Sy, 7, 35-49, 2015.

752     Xu, X. H., Yang, X. S., Miller, D. R., Helble, J. J., and Carley, R. J.: Formulation of bi-directional atmosphere-surface
753     exchanges of elemental mercury, Atmospheric Environment, 33, 4345-4355, Doi 10.1016/S1352-2310(99)00245-9,
754     1999.

755     Yin, R., Feng, X., and Meng, B.: Stable Hg Isotope Variation in Rice Plants (Oryza sativa L.) from the Wanshan Hg
756     Mining District, SW China, Environ. Sci. Technol., 2013.

757     Yuan, H., Dai, Y. J., Xiao, Z. Q., Ji, D. Y., and Shangguan, W.: Reprocessing the MODIS Leaf Area Index products for land

758    surface and climate modelling, Remote Sens Environ, 115, 1171-1187, 2011.

759    Zhang, H., and Lindberg, S. E.: Processes influencing the emission of mercury from soils: A conceptual model, J

760    Geophys Res-Atmos, 104, 21889-21896, 1999.

761    Zhang, H., Lindberg, S. E., and Gustin, M. S.: Nature of diel trend of mercury emission from soil: Current understanding

762    and hypotheses., Abstr Pap Am Chem S, 222, U429-U429, 2001.

763    Zhang, L., Brook, J. R., and Vet, R.: A revised parameterization for gaseous dry deposition in air-quality models,

764    Atmospheric Chemistry and Physics, 3, 2067-2082, 2003.

765    Zhang, L., Blanchard, P., Gay, D. A., Prestbo, E. M., Risch, M. R., Johnson, D., Narayan, J., Zsolway, R., Holsen, T. M.,

766    Miller, E. K., Castro, M. S., Graydon, J. A., St Louis, V. L., and Dalziel, J.: Estimation of speciated and total mercury dry

767    deposition at monitoring locations in eastern and central North America, Atmos Chem Phys, 12, 4327-4340, 2012a.

768    Zhang, L., Blanchard, P., Johnson, D., Dastoor, A., Ryzhkov, A., Lin, C. J., Vijayaraghavan, K., Gay, D., Holsen, T. M.,

769    Huang, J., Graydon, J. A., St Louis, V. L., Castro, M. S., Miller, E. K., Marsik, F., Lu, J., Poissant, L., Pilote, M., and Zhang,

770    K. M.: Assessment of modeled mercury dry deposition over the Great Lakes region, Environ Pollut, 161, 272-283,

771    2012b.

772    Zhang, L., Wang, S. X., Wang, L., Wu, Y., Duan, L., Wu, Q. R., Wang, F. Y., Yang, M., Yang, H., Hao, J. M., and Liu, X.:

773    Updated Emission Inventories for Speciated Atmospheric Mercury from Anthropogenic Sources in China, Environ Sci

774    Technol, 49, 3185-3194, 2015.

775    Zhang, L. X., Hu, Z. M., Fan, J. W., Zhou, D. C., and Tang, F. P.: A meta-analysis of the canopy light extinction coefficient

776    in terrestrial ecosystems, Frontiers of Earth Science, 8, 599-609, 2014.

777    Zhang, Y., Jacob, D. J., Horowitz, H. M., Chen, L., Amos, H. M., Krabbenhoft, D. P., Slemr, F., St. Louis, V. L., and

778    Sunderland, E. M.: Observed decrease in atmospheric mercury explained by global decline in anthropogenic

779    emissions, Proceedings of the National Academy of Sciences, 10.1073/pnas.1516312113, 2016.

780    Zhu, J., Wang, D., Liu, X., and Zhang, Y.: Mercury fluxes from air/surface interfaces in paddy field and dry land, Applied

781    Geochemistry, 26, 10.1016/j.apgeochem.2010.11.025, 2011.

782    Zhu, J., Wang, T., Bieser, J., and Matthias, V.: Source attribution and process analysis for atmospheric mercury in

783    eastern China simulated by CMAQ-Hg, Atmospheric Chemistry and Physics, 15, 8767-8779, 2015a.

784    Zhu, J. S., Wang, D. Y., and Ma, M.: Mercury release flux and its influencing factors at the air-water interface in paddy

785    field in Chongqing, China, Chinese Sci Bull, 58, 266-274, 2013.

786    Zhu, W.: Deployment and Evaluation of Enclosure and Micrometeorological Techniques for Quantifying Air-surface

787    Exchange of Gaseous Elemental Mercury over Agricultural Lands, Doctor of Natural Science, University of Chinese

788    Academy of Sciences, University of Chinese Academy of Sciences, 169 pp., 2014.

789    Zhu, W., Sommar, J., Lin, C. J., and Feng, X.: Mercury vapor air-surface exchange measured by collocated

790    micrometeorological and enclosure methods - Part I: Data comparability and method characteristics, Atmos Chem

791    Phys, 15, 685-702, 2015b.

792    Zhu, W., Sommar, J., Lin, C. J., and Feng, X.: Mercury vapor air-surface exchange measured by collocated

793    micrometeorological and enclosure methods - Part II: Bias and uncertainty analysis, Atmos Chem Phys, 15, 5359-

794    5376, 2015c.

795    Zhu, W., Lin, C. J., Wang, X., Sommar, J., Fu, X., and Feng, X.: Global observations and modeling of atmosphere–surface

796    exchange of elemental mercury: a critical review, Atmos. Chem. Phys., 16, 4451-4480, 10.5194/acp-16-4451-2016,

797    2016.

798

799

800

801 Table 1 Model variables, constants and rate coefficients used in the model simulation.

802

| Term | Description | Values/units | References/Sources |
|---|---|---|---|
| $Hg_1^0$ | $Hg^0$ formed by photo-reduction in solution | ng m$^{-2}$ h$^{-1}$ | |
| $Hg_2^0$ | $Hg^0$ formed by photo-reduction in particles | ng m$^{-2}$ h$^{-1}$ | |
| $Hg_3^0$ | $Hg^0$ formed by the dark-reduction in soil | ng m$^{-2}$ h$^{-1}$ | |
| $K_1$ | Photo-reduction rate in soil solution | s$^{-1}$ | |
| $K_2$ | Photo-reduction rate constant in particles | s$^{-1}$ | |
| $K_3$ | Dark-reduction rate constant in soil | s$^{-1}$ | |
| $Hg_{s,m}$ | $Hg^{II}$ pool in soil pore water | ng m$^{-2}$ | |
| $Hg_{p,m}$ | Reducible $Hg^{II}$ pool in soil particles | ng m$^{-2}$ | |
| $Hg_{t,m}$ | Total reducible $Hg^{II}$ pool in soil | ng m$^{-2}$ | |
| $T$ | Temperature | K | WRF |
| $\theta$ | Soil moisture | % | WRF |
| $R$ | Total solar radiation | W m$^{-2}$ | WRF |
| $BD$ | Soil bulk density | g cm$^{-3}$ | (Shangguan et al., 2013) |
| $LAI$ | Leaf area index | m$^2$ m$^{-2}$ | WRF (Yuan et al., 2011) |
| $[Hg_t]$ | Total $Hg^{II}$ concentration in soil | ng g$^{-1}$ | |
| $V$ | Soil volume | m$^3$ | |
| $kd$ | soil-water partition coefficient | L kg$^{-1}$ | |
| GEM | Atmospheric $Hg^0$ concentration | ng m$^{-3}$ | (Lin et al., 2010b) |
| $\sigma$ | Soil porosity | % | (Shangguan et al., 2013) |
| $D_{soil}$ | $Hg^0$ vapor diffusion coefficient in soil | m$^2$ s$^{-1}$ | |
| $D_0$ | $Hg^0$ vapor diffusion coefficient in ambient air | $1.31\times10^{-5}$ m$^2$ s$^{-1}$ | (Scholtz et al., 2003) |
| $F_{cnp}$ | The flux over canopy biomes | ng m$^{-2}$ h$^{-1}$ | |
| $\Delta t$ | Time duration | s | |
| $R_a$ | Aerodynamic resistance | s m$^{-1}$ | (Wang et al., 2014b;Zhang et al., 2012b) |
| $R_b$ | Quasi-laminar sub-layer resistance | s m$^{-1}$ | Wang et al., 2014b;Zhang et al., 2012b |
| $C_{atm}$ | Atmospheric Hg concentration | ng m$^{-3}$ | Wang et al., 2014b;Zhang et al., 2012b |
| $\chi_{cnp}$ | The total compensation point | ng m$^{-3}$ | Wang et al., 2014b;Zhang et al., 2012b |
| $\chi_c$ | Cuticular interfaces compensation point | ng m$^{-3}$ | Wang et al., 2014b;Zhang et al., 2012b |
| $\chi_s$ | Stomatal interfaces compensation point | ng m$^{-3}$ | Wang et al., 2014b;Zhang et al., 2012b |
| $\chi_g$ | Soil interfaces compensation point | ng m$^{-3}$ | Wang et al., 2014b;Zhang et al., 2012b |
| $R_c$ | cuticular resistance | s m$^{-1}$ | Wang et al., 2014b;Zhang et al., 2012b |
| $R_s$ | stomatal resistance | s m$^{-1}$ | Wang et al., 2014b;Zhang et al., 2012b |
| $R_g$ | soil diffusion resistance | s m$^{-1}$ | Wang et al., 2014b;Zhang et al., 2012b |
| $R_w$ | water diffusion resistance | s m$^{-1}$ | Wang et al., 2014b;Zhang et al., 2012b |
| $R_{g(SO_2)}$ | $SO_2$ soil diffusion resistance | s m$^{-1}$ | Wang et al., 2014b;Zhang et al., 2012b |
| $R_{g(O_3)}$ | $O_3$ soil diffusion resistance | s m$^{-1}$ | Wang et al., 2014b;Zhang et al., 2012b |
| $d$ | Light penetration into soil column | 2.00 mm | (Hebert and Miller, 1990) |

| | | | |
|---|---|---|---|
| $\gamma$ | Ratio of UV radiation over total radiation | 0.08 | (Moan, 2001) |
| $K$ | Canopy light extinction coefficient | 0.56 | (Zhang et al., 2014) |
| $k_r$ | Light extinction coefficient in soil | 3. $mm^{-1}$ | (Ciani et al., 2005) |
| $k_1$ | Photo-reduction rate constant in soil solution | $6.0 \times 10^{-9}$ $m^2$ $W^{-1}$ $s^{-1}$ | (Si and Ariya, 2011) |
| $k_2$ | Photo-reduction rate constant in soil particles | $2.0 \times 10^{-3}$ $m^2$ $W^{-1}$ $h^{-1}$ | (Quinones and Carpi, 2011) |
| $k_3$ | Dark-reduction rate constant in soil | $1.0 \times 10^{-3}$ $h^{-1}$ | (Pannu, 2012) |
| $T_f$ | Reference soil temperature | 32°C(Eq.8), 20°C (Eq. 7,9) | (Pannu, 2012;Quinones and Carpi, 2011) |
| $\theta_f$ | Reference soil moisture | 25% | (Lin et al., 2010a) |
| $r$ | Empirical value from regression | 0.52 | (Lee et al., 2001;Sauve et al., 2000) |
| $s$ | Empirical value from regression | 0.89 | (Lee et al., 2001;Sauve et al., 2000) |
| $t$ | Empirical value from regression | -0.71 | (Lee et al., 2001;Sauve et al., 2000) |
| $\varphi$ | Ratio of reducible Hg in soil | 0.003 (bare), 0.03(others) | (Pannu, 2012) |
| $\alpha_{Hg^0}$ | Scaling factor of reactivity Hg | 0 | (Wang et al., 2014b) |
| $\beta_{Hg^0}$ | Scaling factor of reactivity Hg | 0.1 | (Wang et al., 2014b) |
| $Hg_w^{2+}$ | $Hg^{II}$ concentration on leaf | 3 ng $m^{-2}$ leaf | (Laacouri et al., 2013) |

803

804    Table 2 Examined model variables and the experimental levels of factorial design for air-soil exchange.

805

| Terms | Description | Low level | High level |
|---|---|---|---|
| BD | Soil bulk density (g cm$^{-3}$) | 0.1 | 1.5 |
| pH | Soil pH (dimensionless) | 4 | 9 |
| P | Soil total porosity (%) | 0.05 | 0.5 |
| T | Soil temperature (ºC) | 0 | 35 |
| SMOIS | Soil moisture (%) | 0.05 | 0.5 |
| R0 | Solar irradiance above canopy (w m$^{-2}$) | 0 | 1000 |
| LAI | Leaf area index (dimensionless) | 0 | 7 |
| GEM | Atmospheric Hg0 concentration (ng m$^{-3}$) | 1.5 | 5 |
| Hgs | Hg concentration in soil (ng g$^{-1}$) | 10 | 400 |
| Foc | Soil organic matter content (%) | 0.5 | 30 |
| k1 | photo-reduction rates in soil solution (m$^2$ W$^{-1}$ s$^{-1}$) | $3 \times 10^{-9}$ | $9 \times 10^{-9}$ |
| k2 | photo-reduction rates in soil particles (m$^2$ W$^{-1}$ h$^{-1}$) | $0.7 \times 10^{-3}$ | $3.0 \times 10^{-3}$ |
| k3 | Non-photo-reduction rates (thermal, h$^{-1}$) | $1.0 \times 10^{-3}$ | $2.3 \times 10^{-3}$ |

806

807 Table 3. Mean annual air-surface fluxes, and annual total Hg emissions from individual landuse. SHg is the
808 Hg content in surface soil (0-10 cm), FF is the $Hg^0$ flux over foliage, and FS is the $Hg^0$ flux over soil.
809

| Type | Description | Area(%) | SHg (ng g$^{-1}$) | FF (ng m$^{-2}$ h$^{-1}$) | Leaf(Mg) | FS(ng m$^{-2}$ h$^{-1}$) | Soil(Mg) | Tot(Mg) |
|---|---|---|---|---|---|---|---|---|
| C1 | Evergreen needleleaf forest | 5.7 | 186±74 | -2.8 | -13.5 | 6.9 | 35.2 | 21.7 |
| C2 | Evergreen broadleaf forest | 2.6 | 184±35 | -2.6 | -6.5 | 6.2 | 16.1 | 9.5 |
| C3 | Deciduous needleleaf forest | 0.1 | 119±9 | -0.2 | -0.03 | 0.7 | 0.1 | 0.1 |
| C4 | Deciduous broadleaf forest | 3.3 | 143±47 | -1.2 | -3.7 | 2.7 | 8.3 | 4.6 |
| C5 | Mixed forest | 2.4 | 211±83 | -2.2 | -4.5 | 4.7 | 10.5 | 6.0 |
| C6 | Closed shrubland | 5.2 | 115±77 | -3.2 | -14.1 | 5.6 | 26.0 | 11.9 |
| C7 | Open shrubland | 0.6 | 155±72 | -1.4 | -0.7 | 10.8 | 6.5 | 5.7 |
| C8 | Woody savanna | 0.3 | 197±96 | -4.5 | -1.0 | 12.9 | 3.2 | 2.2 |
| C9 | Savanna | 0.0 | 157±47 | -0.6 | -0.003 | 0.1 | 0.0 | 0.0 |
| C10 | Grassland | 31.8 | 61±33 | -0.8 | -20.3 | 8.0 | 221.8 | 201.4 |
| C11 | Permanent wetland | 1.1 | 74±24 | -0.8 | -0.8 | 9.8 | 10.0 | 9.2 |
| C12 | Cropland | 20.5 | 80±59 | -1.8 | -31.6 | 10.0 | 179.0 | 147.5 |
| C13 | Cropland mosaic | 1.6 | 82±74 | -2.0 | -3.0 | 6.7 | 10.1 | 7.2 |
| C14 | Urban land | 0.2 | 162±83 | -3.6 | -0.7 | 23.3 | 4.4 | 3.7 |
| C15 | Snow and ice | 0.8 | 31±15 | | | 2.0 | 3.1 | 3.1 |
| C16 | Barren vegetated land | 21.6 | 35±7 | | | 1.5 | 22.2 | 22.2 |
| C17 | Bodies of water | 2.2 | | | | 3.4 | 9.0 | 9.0 |
| Sum | | 100.0 | | | -100.4 | | 565.5 | 465.1 |

810
811

812 Table 4. Pearson correlations between mean total fluxes and major controlling environmental parameters
813 in each season. "**" means $p < 0.01$ and "*" means $p < 0.05$.

814

815

| Term | Winter | Spring | Summer | Autumn |
|---|---|---|---|---|
| LAI | -0.14[*] | -0.24[**] | -0.39[**] | -0.30[**] |
| Soil temperature | 0.27[**] | 0.35[**] | 0.54[**] | 0.38[**] |
| Solar radiation | 0.27[**] | 0.32[**] | 0.59[**] | 0.36[**] |
| Soil Hg concentration | 0.47[**] | 0.13[*] | 0.02 | 0.39[**] |
| Soil bulk density | 0.41[**] | 0.16[*] | 0.04 | 0.32[**] |
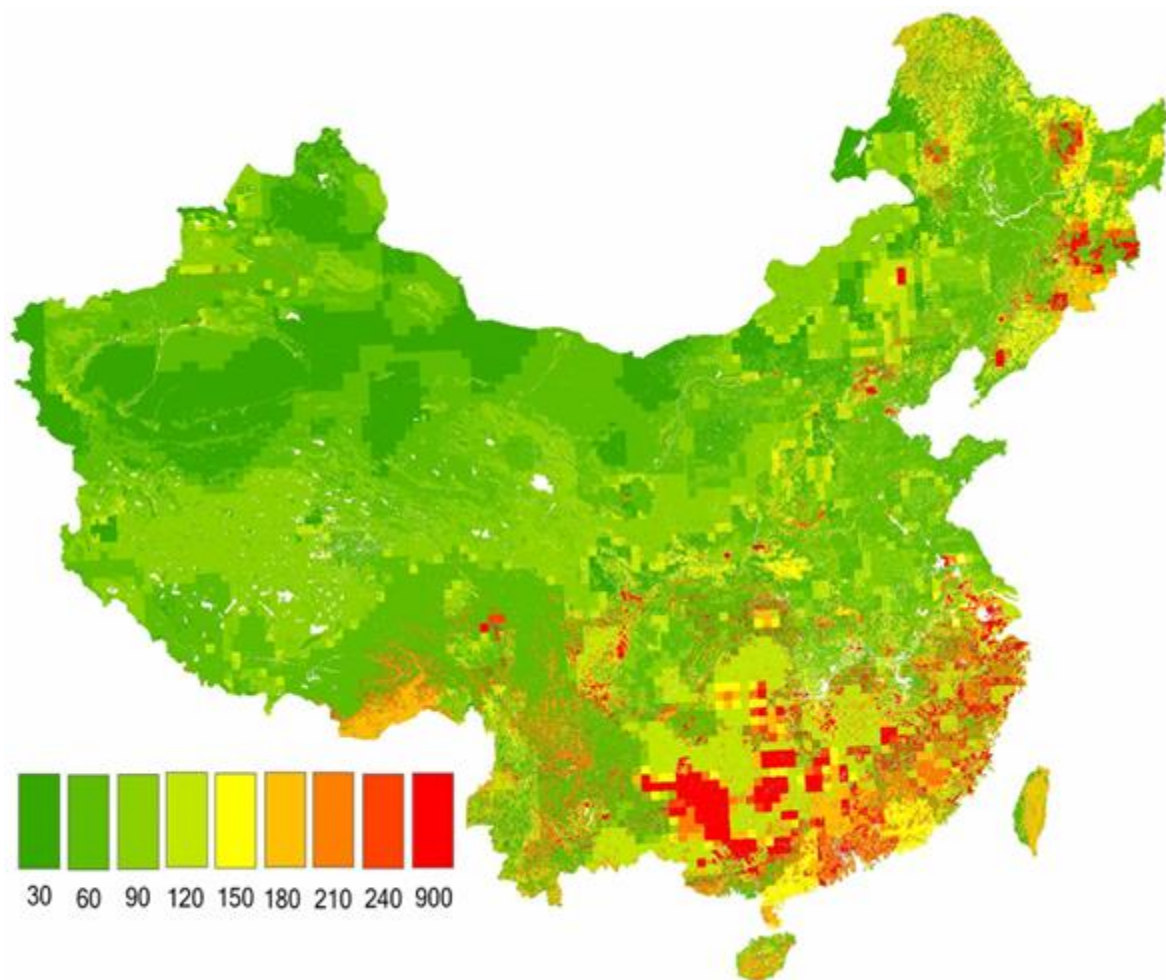
816

817 Figure 1. Updated Hg concentrations (ng g$^{-1}$) in surface soil (0-20 cm) of China. Sampling areas in

818 NMPRGS covers most agriculturally and industrially developed regions of eastern and central China, and

819 is presented in more details in Li et al. (2014).

820
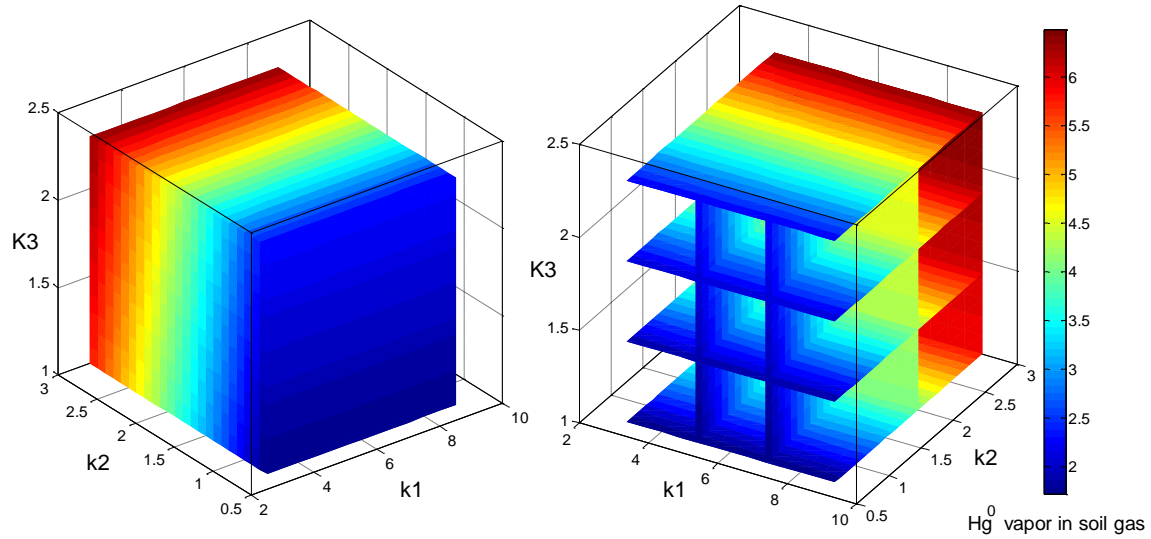
821

822  Figure 2. Variation of $Hg^0$ concentrations (ng m$^{-3}$) in the forest soil pore gas using the typical ranges of

823  kinetic constants for $Hg^{II}$ reduction in soil (see text for details): $k_1 = 3.0\text{-}9.0 \times 10^{-9}$ m$^2$ W$^{-1}$ s$^{-1}$, $k_2 = 0.7\text{-}3.0 \times 10^{-1}$

824  $^3$ m$^2$ W$^{-1}$ h$^{-1}$, $k_3 = 1.0\text{-}2.3 \times 10^{-3}$ h$^{-1}$, soil Hg content=150 ng g$^{-1}$, pH=4, soil organic content = 20%, soil bulk

825  density = 0.8 g m$^{-3}$, solar irradiance = 1000 W m$^{-2}$, soil temperature = 25 $^o$C, LAI = 5 m$^2$ m$^{-2}$, soil moisture

826  content = 20%, and soil soil porosity = 40%. The environmental conditions are similar to conditions

827  reported by Moore and Castro (2012).
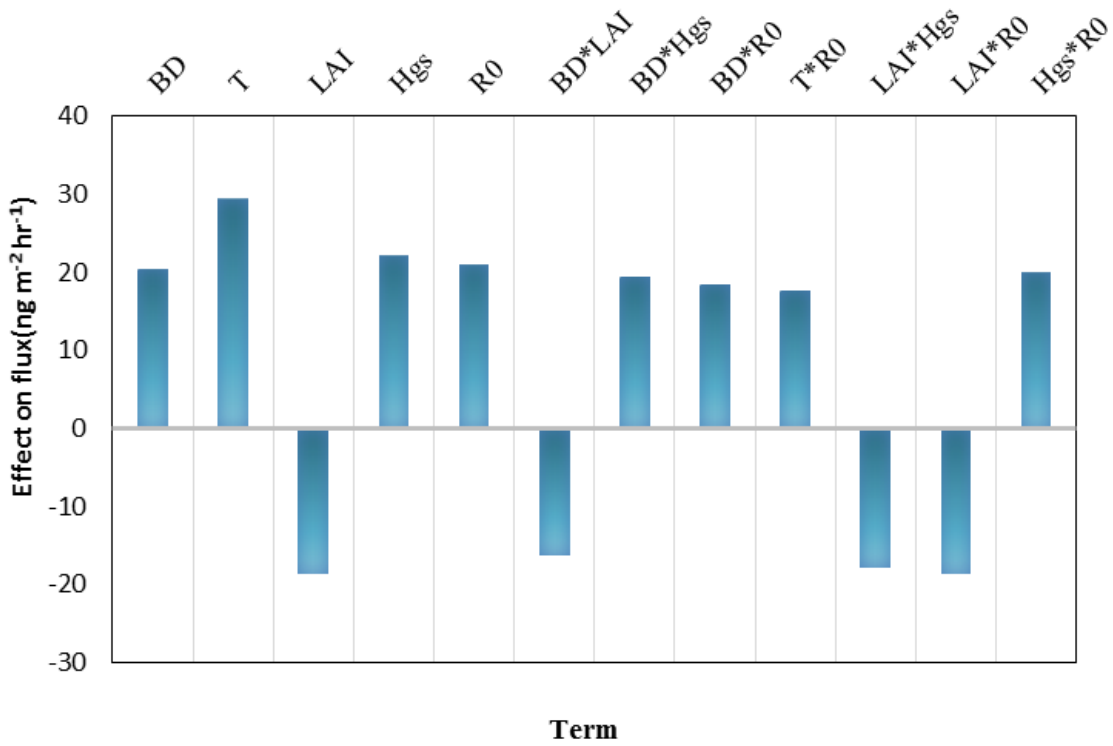
828

829 Figure 3. Sensitivity analysis on model parameters for air-soil exchange using a 2-level factorial design
830 after pre-screening the model variables shown in Table 2 for the identified significant factors. The effects
831 shown in the figure are based on a significance level of 95% (i.e., $p<0.05$).
832

833

834
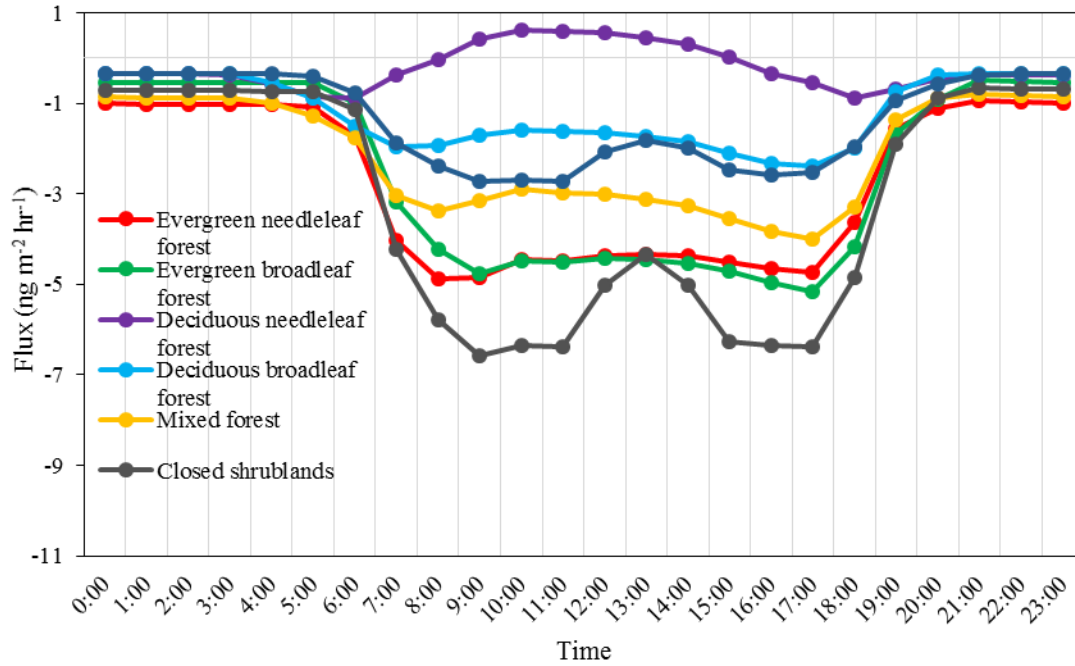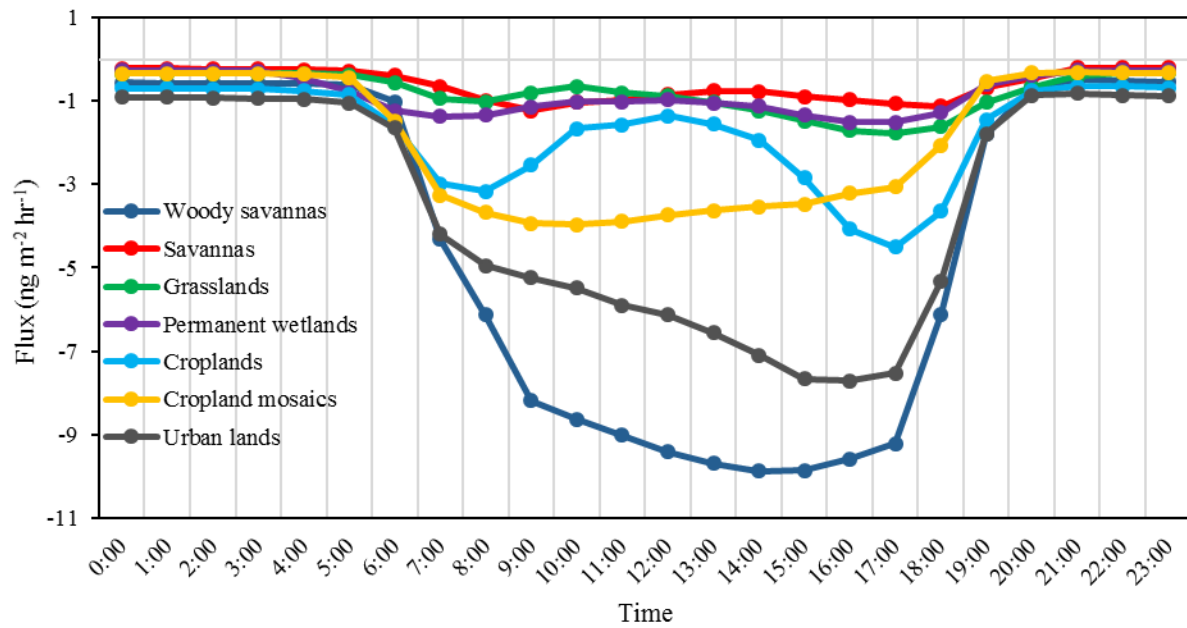
Figure 4. Diurnal variation of mean simulated exchange fluxes of Hg$^0$ over canopy in the model domain
(UTC+8).

837

838

839

840
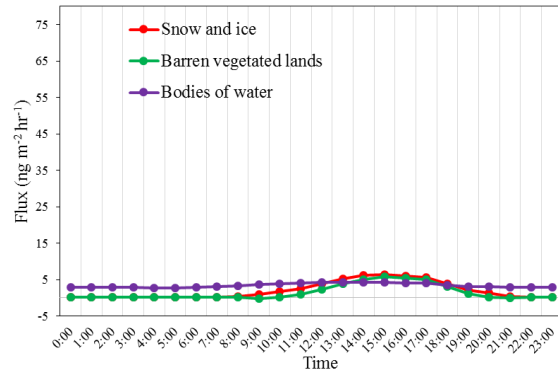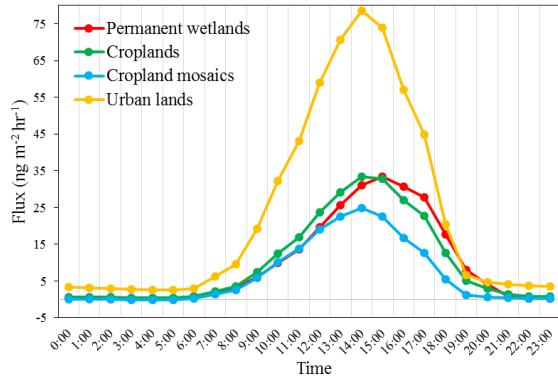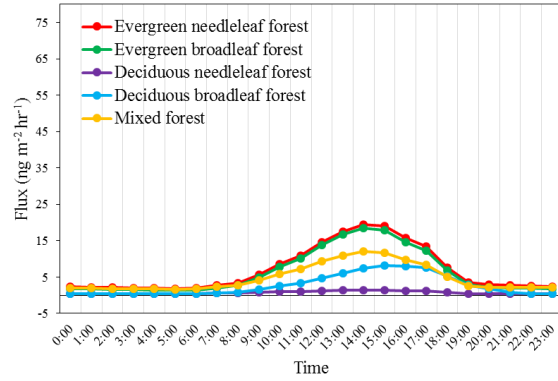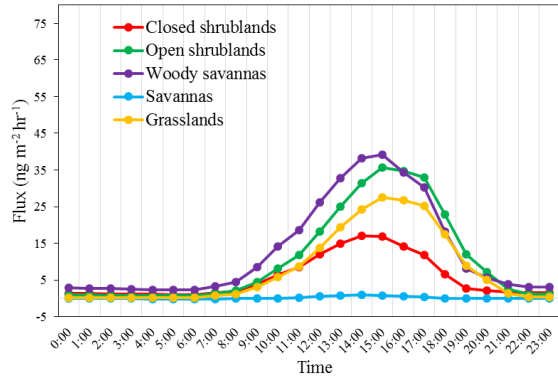
841 Figure 5. Diurnal variation of mean simulated exchange fluxes of Hg$^0$ over soil and water surfaces in the

842 model domain (UTC+8).

843
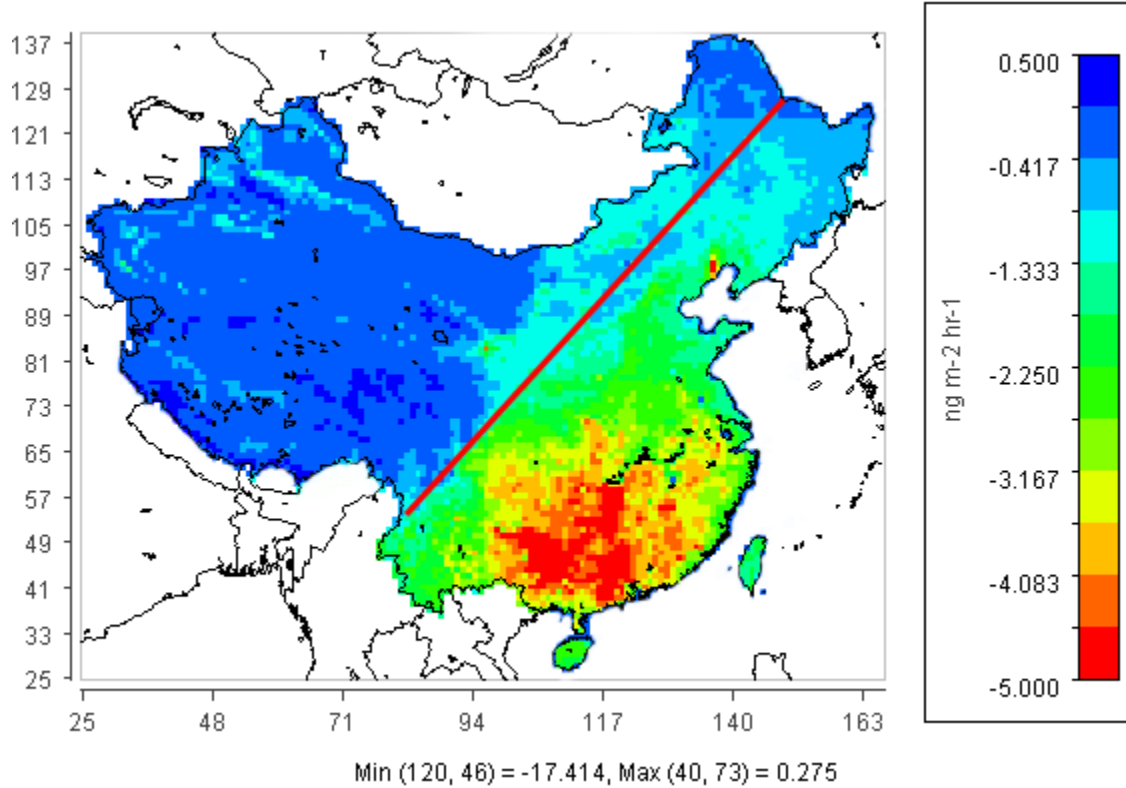
844
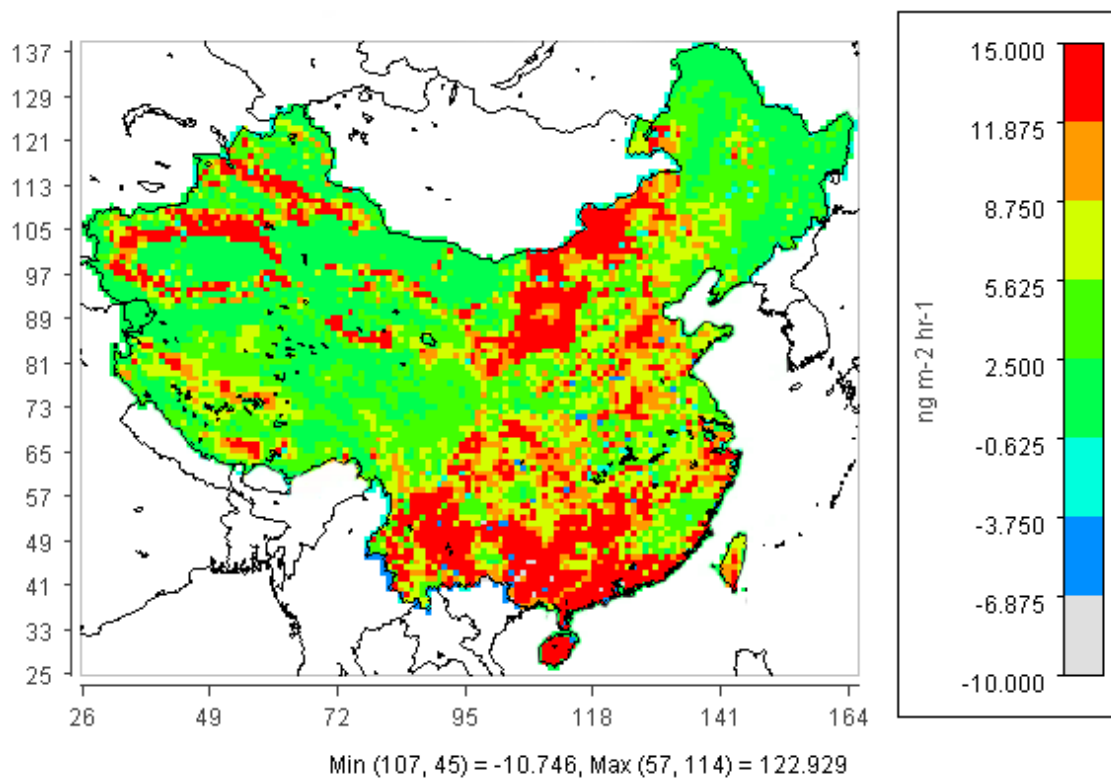
845

846 Figure 6. Simulated results of (1) mean annual air-foliage flux, and (2) mean annual air-soil flux in the

847 study domain.

848

849

850

851
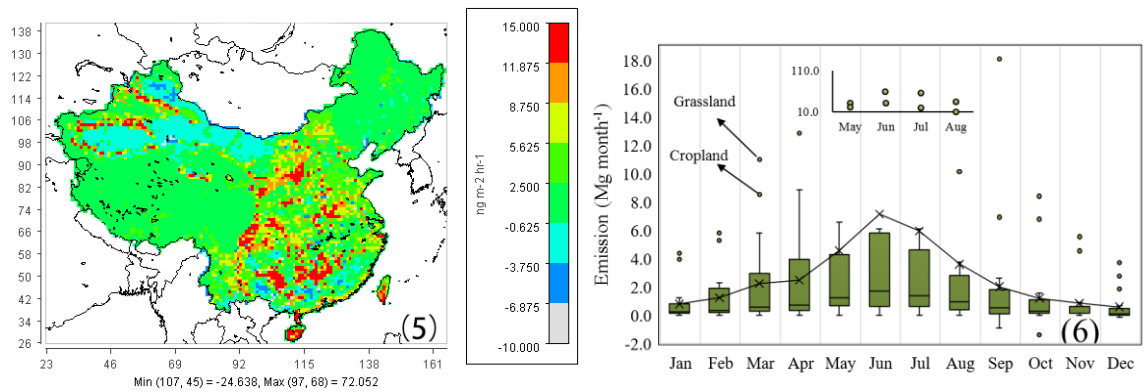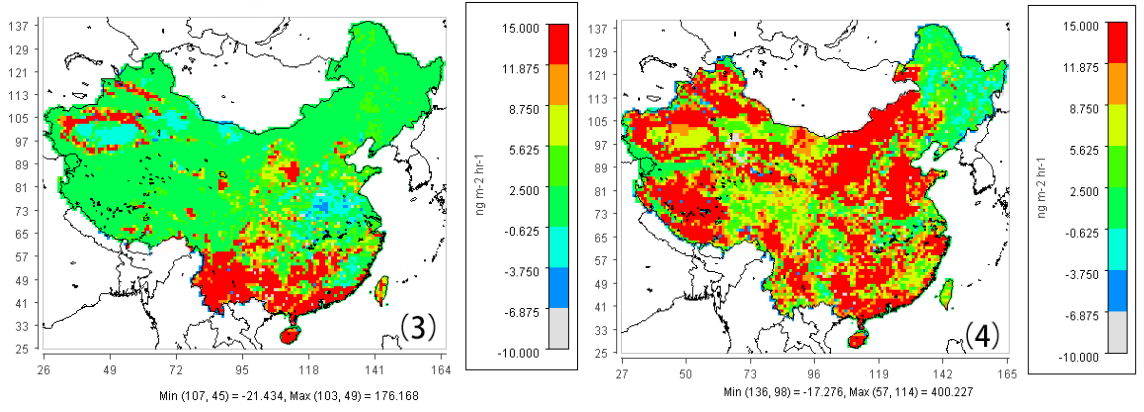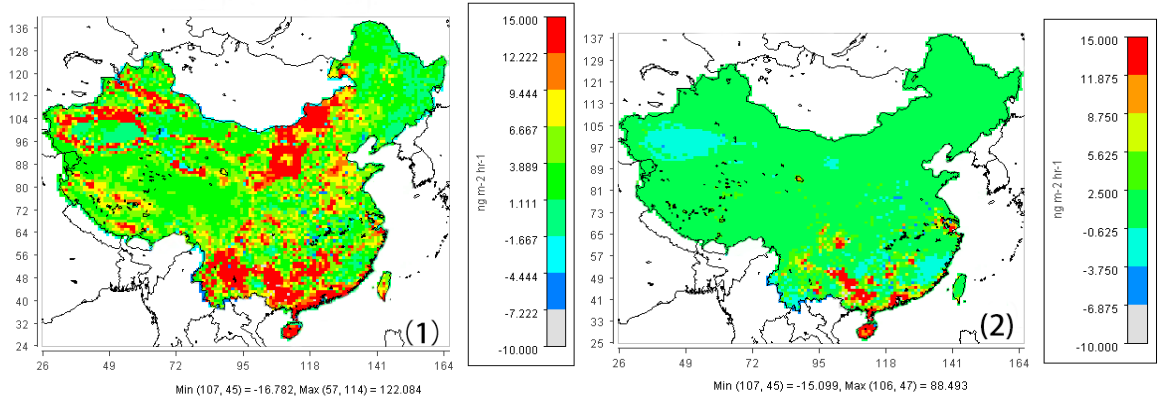
Figure 7. Model estimates of (1) annual mean Hg$^0$ fluxes in the model domain; (2) seasonal mean Hg$^0$ fluxes in winter, (3) seasonal mean Hg$^0$ fluxes in spring, (4) seasonal mean Hg$^0$ fluxes in summer, (5) seasonal mean Hg$^0$ fluxes in autumn, and (6) monthly Hg$^0$ fluxes in the grid cells (box and whisker chart showing maximum, 75$^{th}$ percentile, mean, median, 25$^{th}$ percentile, and minimum).

856
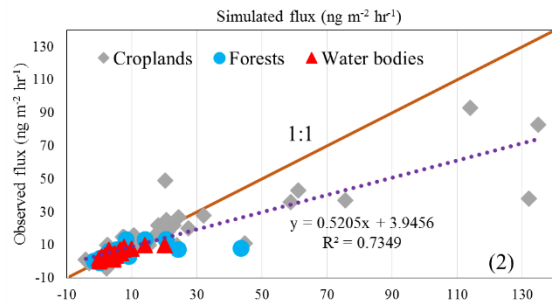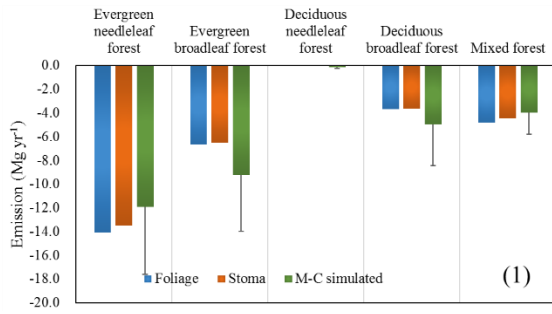
857
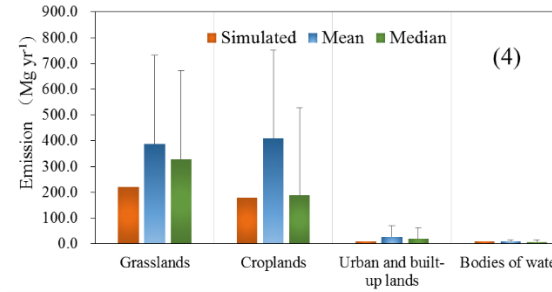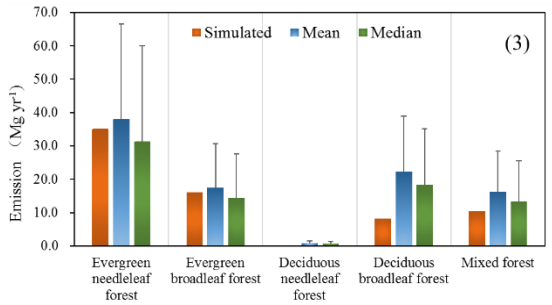
858

859    Figure 8. Model verification: (1) model estimates of $Hg^0$ uptake by foliage (which include the uptake by
860    stoma less the re-emission and from cuticle) and by stoma, compared to the estimate (mean and 95%
861    confidence interval) of $Hg^0$ uptake using Monte Carlo (M-C) simulation of the observational data; (2)
862    scatter plot of the observed fluxes vs. simulated fluxes for different landuses (the flux observations are
863    described in detailed in Table S2), (3) comparison between simulated exchange and measured exchange
864    over soil under canopy, and (4) comparison between simulated exchange and measured exchange over
865    grasslands, cropland and water surface. The mean and median of Figures 10.3 and 10.4 are based on the
866    filed data from peer-review literatures (n=19 for forests; n=12 for grasslands; n=42 for croplands; n=51 for
867    water bodies). Note that the exchange over deciduous needleleaf forests in Figure 8.1 is small because of
868    the small forest area.